Supporting Information for

Exploring the Enantioselective Synthesis Mechanism of Ammonium Cations in Solution Using Deep Learning Potential

Hongqiang Cui,[†,‡] Da Zheng,[†,‡] Huiying Chu, [*,†,§] Yan Li,[*,†,§] Guohui Li[*,†,§]

[†]State Key Laboratory of Chemical Reaction Dynamics, Dalian Institute of Chemical Physics, Chinese Academy of Sciences, Dalian 116023, China

[‡]University of Chinese Academy of Sciences, Beijing 100049, China

[§]Interdisciplinary Research Center for Biology and Chemistry, Liaoning Normal University, Dalian, Liaoning 116029, China

Computational Methods

Investigation of the mechanisms based on the DFT calculations

DFT calculations are performed to investigate the mechanisms revealed by DLPMD simulations. All calculations are conducted using the Gaussian 16 software package.[1] Geometry optimizations of all stationary points are performed at the B3LYP/6-31G(d,p) level of theory.[2-4] Frequency calculations and single point energy calculations are performed at the same level to verify whether the stationary points are minima (zero imaginary frequency) or saddle points (only one imaginary frequency). The solvation effects of five solvents, including dimethyl sulfoxide (DMSO), methanol, chloroform, carbon tetrachloride (CTC), and cyclohexane, are evaluated separately using the solvation model based on density (SMD).[5] Relative energies calculated by DFT methods in chloroform, which was used as the experimental solvent[6], are shown in Fig. S5. Additional results for the other solvents are summarized in Table S2 to elucidate the influence of different solvation environments.

The Binding Energy between allyl bromide and Solvent Molecules

DFT calculations are conducted to evaluate the binding energies between allyl bromide and various solvent molecules. All calculations are performed using the Gaussian 16 software package.[1] In this study, five solvents are selected: dimethyl sulfoxide (DMSO), methanol, chloroform, carbon tetrachloride (CTC), and cyclohexane (Fig. S6). For each solvent, 100 initial structures are generated by randomly placing a solvent molecule within a 5 Å radius around the bromine atom of allyl bromide. These 100 binding structures, as well as the isolated allyl bromide and solvent molecules, are individually optimized at the B3LYP/6-31G(d,p) level of theory.[2-4] Frequency calculations and single point energy calculations are performed at the same level to verify that the stationary points are minima (0 imaginary frequency). DFT calculations are performed using the SMD model[5] to account for solvent effects. For each solvent type (DMSO, methanol, chloroform, CTC, and cyclohexane), the energies of the binding structures, the isolated allyl bromide molecule, and the isolated solvent molecule are computed separately in their respective solvation environments. The corresponding dielectric constants are listed in Fig. S6a. Representative binding structures are selected from the 100 optimized structures using the K-means clustering method[7, 8] based on RMSD. The maximum RMSD value allowed between structures within the same cluster is set to 1.5 Å. Prior to RMSD calculations, all binding structures are aligned based on the atoms of the allyl bromide molecule to eliminate translational and rotational differences. For RMSD calculations used in clustering analysis, different atoms are selected for each solvent molecule to capture the structural features relevant to binding. Specifically, two carbon atoms, one sulfur atom, and one oxygen atom are selected for DMSO; one carbon atom and one oxygen atom for methanol; one carbon atom and one hydrogen atom for chloroform; one carbon atom for carbon tetrachloride (CTC); the center of six carbon atoms for cyclohexane. These selected atoms define the solvent molecular orientation and ensure meaningful structural comparisons across the optimized configurations. The binding energy is

defined as Equation (S1):[9-11]

$$\Delta E = E_{allylBromide-solvent} - E_{allylBromide} - E_{solvent} \quad \text{(S1)}$$

Where ΔE denotes the binding energy, $E_{allylBromide\text{-}solvent}$ is the total energy of the optimized binding structure, $E_{allylBromide}$ is the energy of isolated allyl bromide, $E_{solvent}$ is the energy of isolated solvent molecule.

Molecular Dynamics Simulations based on hybrid functionals

MD simulations are performed using cp2k-7.2.[12] Molecular dynamics simulations were performed on 16 systems with sizes ranging from 380 to 550 atoms. 50 fs simulations are performed with a time step size of 0.5 fs in the NVT ensemble with PBCs. All MD simulations are conducted at 323 K using CSVR thermostat with a damping constant of 10 fs. Energies and forces are computed using the DZVP-MOLOPT-SR-GTH basis set[13] along with GTH-PBE pseudopotentials.[14-16] The exchange-correlation energy was described with the PBE0 hybrid functional[17] and the dispersion-corrected DFT-D3 scheme with Becke-Johnson damping (DFT-D3(BJ)) was employed for dispersion correction. [18, 19] In parallel, the same basis set and dispersion correction are applied with the Heyd-Scuseria-Ernzerhof (HSE06) functional[20, 21] to ensure consistency in comparison. The auxiliary density matrix method (ADMM)[22] was applied with admm-dzp as the auxiliary basis set. In addition, for the 16 systems, 50 fs simulations are also performed using the PBE functional,[23] with the computational parameters identical to those adopted in the active learning workflow of this study.

Table S4 summarizes the average computational wall time for the sixteen systems, providing a comparison of the computational efficiency of simulations performed with the PBE, PBE0, and HSE06 functionals.

Addition Results

DFT calculations of the mechanisms

To investigate the impact of solvent effects on the energy barriers of different reaction pathways, the detailed reaction mechanisms of the three types of reaction pathways a-c (Fig. 1a, 1b, and 1c) are investigated using DFT calculations at B3LYP/6-31G(d, p)[2-4] level of theory. TS1S, TS2S and TS3S (their enantiomeric counterparts, TS1R, TS2R and TS3R) are transition states corresponding to the three reaction pathways a-c (Fig. 1a, 1b, and 1c). The solvent effects are modeled using implicit solvation model SMD[5] (Fig. S5a). The reaction pathways towards the NR_4^+ (R) are mirror images of those towards NR_4^+ (S). Therefore, the analysis focuses only on reaction pathways towards NR_4^+ (S). TS1S is 11.7 and 11.8 kcal/mol higher in energy than TS2S and TS3S (Fig. S5a), respectively, suggesting that the bromine atom hinders the nucleophilic attack of the nitrogen atom on the carbon atom. This indicates that the reaction pathway a (Fig. 1a) is unfavorable. TS2S is only 0.1 kcal/mol higher than TS3S (Fig. S5a), suggesting that the reaction pathways b-c (Fig. 1b and 1c) are competitive.

For other solvent environments, as shown in Table S2, TS1S consistently exhibits

higher energy than both TS2S and TS3S, further supporting the steric hindrance effect of the bromine atom. Notably, the barrier for TS3S is 1.9 and 2.3 kcal/mol higher than that for TS2S in highly polar solvents such as DMSO and methanol. In contrast, TS3S and TS2S exhibit nearly identical barriers in weakly polar solvents such as chloroform, CTC, and cyclohexane. These findings highlight the importance of accounting for solvent effects in this reaction system.

The Binding Energy between allyl bromide and Solvent Molecules

The 100 optimized binding structures for DMSO, methanol, chloroform, CTC, and cyclohexane are grouped into 55, 43, 39, 18, and 17 clusters, respectively. In addition, the five lowest-energy binding structures for each solvent are presented in Fig. S6b.

Evaluation of the Accuracy and Efficiency of DFT Methods

The reliability of DLP models critically depends on the completeness of conformational space sampling within the training dataset. Consequently, when constructing PESs using deep learning methods, sampling efficiency serves as a key metric for evaluating computational chemistry methods. While hybrid functionals generally offer higher accuracy than generalized gradient approximation (GGA) functionals, their substantially higher computational cost represents a major limitation. In previous studies, the PBE functional has been widely applied,[24-27] as it provides a favorable compromise between computational accuracy and efficiency.[28] To explore the potential of incorporating higher-accuracy hybrid functionals, such as PBE0 and HSE06, into future workflows, it is necessary to assess both their computational efficiency and the extent of accuracy improvement relative to PBE.

In this study, 16 systems with sizes ranging from 380 to 550 atoms are employed to evaluate the computational efficiency of PBE0 and HSE06 functionals. As shown in Table S4, energy calculations using these hybrid functionals require roughly five times the computational wall time of calculations based on PBE functional, while MD simulations demand approximately sixteen times longer. It should be emphasized that initial guess wavefunctions generated with PBE are essential to avoid self-consistent field (SCF) convergence failures in calculations based on PBE0 and HSE06. Therefore, if PBE provides a reasonable description of the PESs, the use of higher-accuracy hybrid functionals should be limited to cases where improved accuracy is critical.

To assess the accuracy of PBE, PBE0, and HSE06 in describing reaction pathways observed during the active learning workflow, structures along pathways a-d (Fig. 1a-d) are labeled using all three functionals. Notably, the reaction pathways leading to NR_4^+ (R) (Fig. S1a-d) are mirror images of those leading to NR_4^+ (S) (Fig. 1f-i). Therefore, only structures along pathways toward NR_4^+ (S) are considered. All calculations are performed using the DZVP-MOLOPT-SR-GTH basis set and the DFT-D3(BJ) dispersion correction. The energetics along the reaction pathways, calculated using different DFT methods, are shown in Fig. S25.

Firstly, the three functionals predict nearly identical transition state locations along pathways a-c and identify pathway d as physically implausible. Secondly, regarding relative energies along pathways a-c, the PBE functional shows deviations compared

with results obtained using the PBE0 and HSE06 functionals. For both the PBE functional with and without the DFT-D3(BJ) dispersion correction, the energy barrier of pathway a is consistently underestimated. For pathways b-c, the PBE functional without DFT-D3(BJ) overestimates the relative energy of the product state (NR_4^+Br), whereas DFT-D3(BJ) dispersion correction stabilizes the product state but underestimates the transition states. Nevertheless, all three DFT functionals identify reaction pathway c as the most favorable, whereas pathway a is unfavorable compared with pathways b and c. Despite quantitative differences in the relative energies, the PBE functional without DFT-D3(BJ) is still able to correctly reproduce the relative energy ordering of the reactants, products, and transition states along each pathway, in good agreement with the PBE0 and HSE06 results. Thirdly, although the DLP model is pre-tuned using structures along reaction pathways labeled by the PBE functional, its prediction of the product-state relative energy (NR_4^+Br) along reaction pathways b-c is consistent with PBE0 and HSE06 functionals, unlike the PBE functional. This discrepancy primarily arises from the composition of the training dataset. As shown in Methods section (Deep Potential Descriptor and Training), in the second stage, the DLP model is trained using a dataset that includes 1,202 structures corresponding to these key reaction pathways labeled using DFT calculations in vacuum and 173,857 structures derived from AIMD trajectories performed with explicit solvent molecules. The overestimation of the relative energy of the product state (NR_4^+Br) by the PBE functional without DFT-D3(BJ) appears to be partially corrected by the structures derived from AIMD trajectories. In general, the PBE functional provides a suitable balance between computational efficiency and accuracy in this study.

For unknown reaction systems in future work, GGA functionals (e.g., PBE) remain the preferred choice, as they not only provide a favorable balance between computational efficiency and accuracy but also indispensable for generating the initial guess wavefunctions required for high-accuracy hybrid functional calculations. Reaction pathways identified in AIMD and DLPMD simulations should be evaluated using both GGA and hybrid functionals. If GGA fails to correctly distinguish relative energies between pathways, high-level hybrid functionals are required for training dataset construction. However, this implies that the training dataset constructed using MD simulations based on GGA functional would need to be re-labeled using a higher-accuracy hybrid functional. Consequently, to minimize computational costs, semi-empirical simulations can be used in place of DFT-based simulations. The structures generated in simulations based on semi-empirical methods can then be re-labeled using a GGA functional. If replacement with higher-accuracy hybrid-labeled structures is necessary, the wavefunctions obtained during the GGA labeling process can serve as the initial guess for the hybrid functional calculations. This procedure is essential to avoid SCF convergence failures. Further optimization strategies for active learning workflow require explorations in future studies.

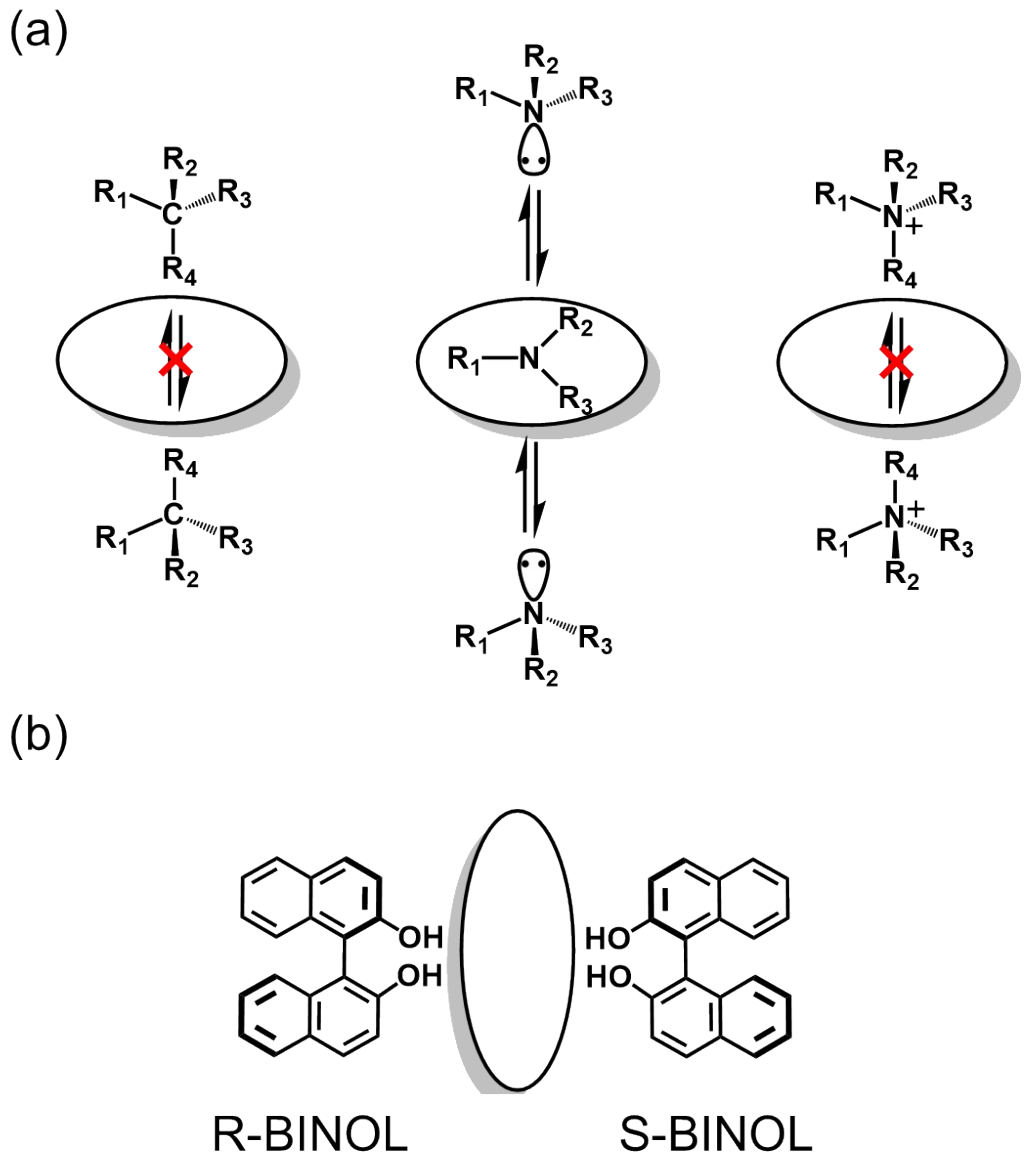

Scheme S1. (a) Comparison of the stability of carbon- and nitrogen-based stereocenters. Carbon stereocenters are both configurationally and conformationally stable, whereas amines exhibit conformational instability due to nitrogen inversion. Quaternization of amines to form ammonium salts stabilizes the nitrogen center. (b) Catalyst molecules used in experiment.[6]

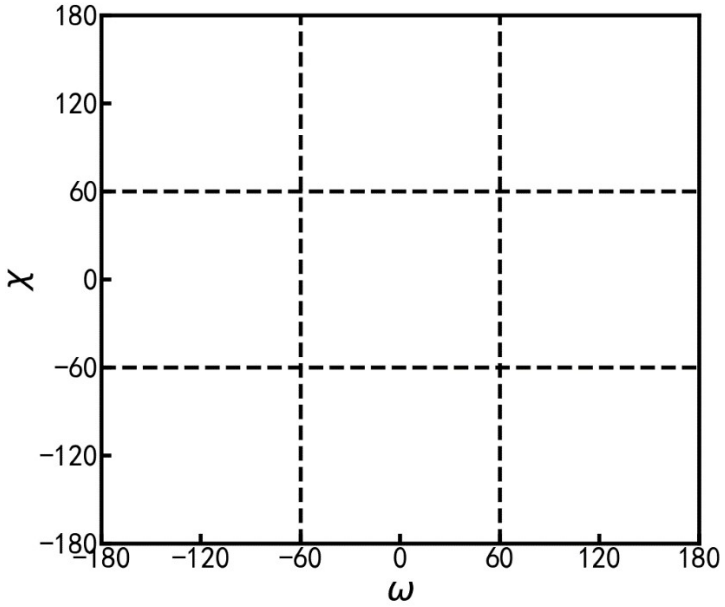

Scheme S2. Nine parts of the spatial dimension.

Table S1. Number of occurrences of the five reaction pathways a-e (Fig. 1a-e) in five simulations shown in Fig. S4.

	R-BINOL										S-BINOL									
Simulation Index	R					S					S					R				
	e	d	c	b	a	a	b	c	d	e	e	d	c	b	a	a	b	c	d	e
1	3	0	0	1	0	0	8	1	0	2	1	0	0	4	0	0	6	0	0	1
2	0	0	0	7	0	0	5	0	0	0	0	0	0	6	0	0	7	0	0	1
3	1	0	0	5	0	0	6	3	0	0	0	0	0	3	1	0	12	3	0	0
4	0	0	0	4	0	0	8	0	0	0	0	0	0	8	0	0	7	1	0	0
5	0	0	0	2	0	0	6	1	0	2	0	0	0	4	0	0	6	0	0	0

Notes: Reaction types a, b, c, d, e shown in Table S1 correspond to the reaction pathways a-e (Fig. 1a-e).

Table S2. Relative Gibbs free energies of the species shown in Fig. S5a calculated using SMD models with varying dielectric constants.

R-BINOL						
Solvent (Dielectric Constants)	Sub (kcal/mol)	SubHS (kcal/mol)	TS1S (kcal/mol)	TS2S (kcal/mol)	TS3S (kcal/mol)	ProS (kcal/mol)
DMSO (46.83)	0.0	15.0	46.0 (10.1)	34.0 (-1.9)	35.9 (0.0)	16.6
Methanol (32.61)	0.0	15.7	46.1 (9.8)	34.0 (-2.3)	36.3 (0.0)	16.8
Chloroform (4.71)	0.0	12.9	48.2 (11.8)	36.5 (0.1)	36.4 (0.0)	21.2
CTC (2.23)	0.0	12.5	49.7 (11.4)	38.2 (-0.1)	38.3 (0.0)	25.0
Cyclohexane (2.02)	0.0	12.0	49.8 (12.0)	38.0 (0.2)	37.8 (0.0)	25.3

Notes: Gibbs free energies relative to Sub are labeled in black, while those relative to TS3S are labeled in red.

Table S3. The MAEs of structures without charge and structures with charge.

(A) Structures without charge		
	MAEs	
Number of structures	Energy (eV/Natoms)	Force (eV/ Å)
7467	0.00729	0.03840
(B) Structures with charge		
	MAEs	
Number of structures	Energy (eV/Natoms)	Force (eV/ Å)
5025	0.01823	0.04331

Table S4. Computational average wall time for 16 systems across DFT methods and Tasks.

DFT (Task)	PBE (Energy)	PBE0 (Energy)	HSE06 (Energy)	PBE (50 fs MD)	PBE0 (50 fs MD)	HSE06 (50 fs MD)
Average Wall Time (hours)	0.020	0.098	0.099	0.467	7.509	7.512

Notes: "Energy" represents tasks for computing system energies using DFT methods, "50fs MD" represents tasks for performing 50 fs MD simulations using DFT methods. All calculations are performed using 64 CPU cores.

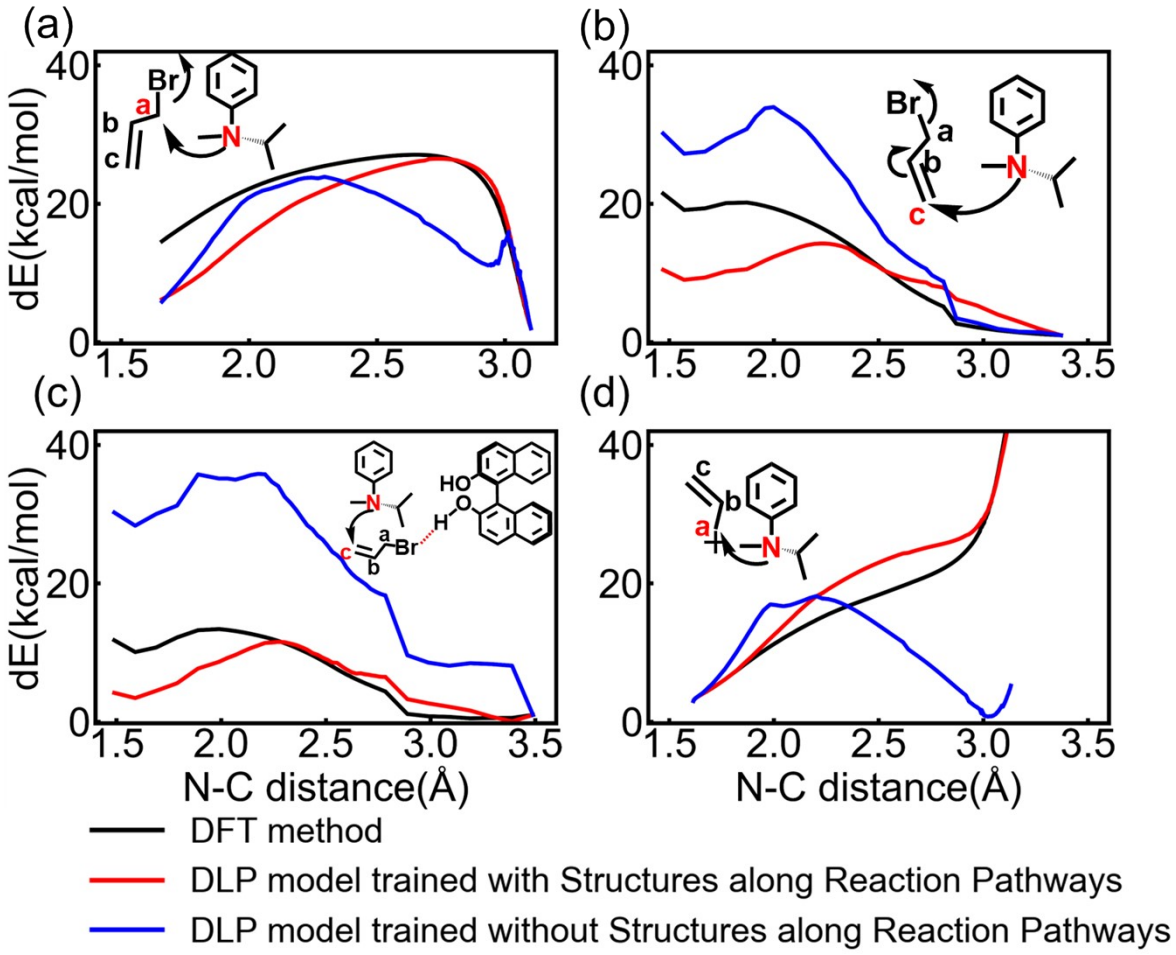

Fig. S1. Energetics along the N-C distances are calculated using the DLP model for $NR_4^+(R)$ structures optimized at the PBE/DZVP-MOLOPT-SR-GTH level of theory. (a-d): Reaction coordinate diagrams corresponding to the reaction pathways a-d (Fig. 1a-d), respectively. **Notes:** In Fig. S1a-d, the horizontal axis represents the distance between the nitrogen and carbon atoms, both labeled in red.

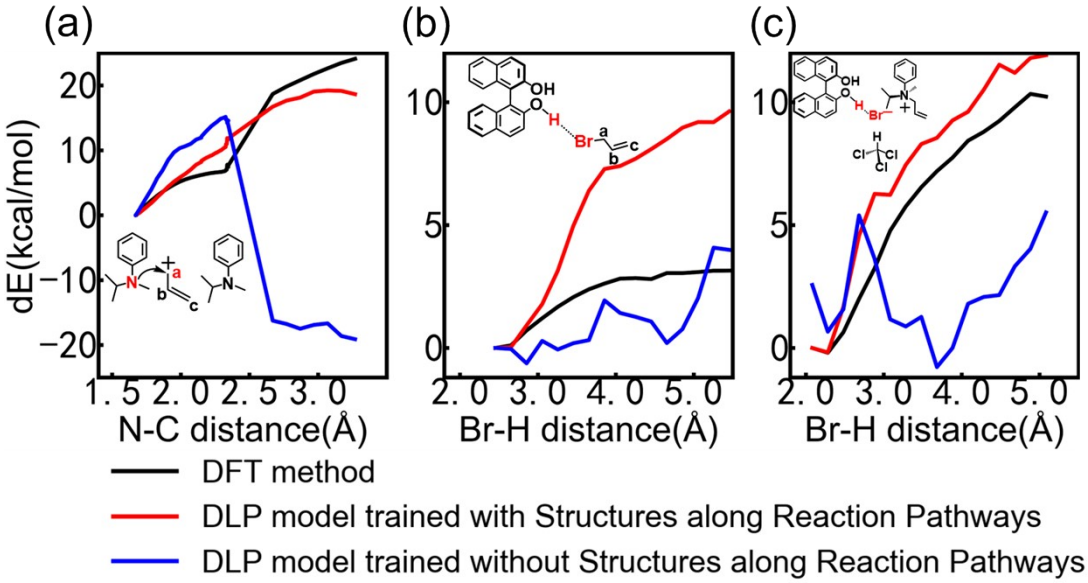

Fig. S2. Energetics along the N-C distances calculated using the DLP model for NR_4^+ structures optimized at the PBE/DZVP-MOLOPT-SR-GTH level of theory. (a) Reaction coordinate diagram corresponding to the reaction pathway e (Fig. 1e). Energetics along the distance between the bromine atom and the hydrogen atom in the hydroxyl group calculated using the DLP model for structures optimized at the same level of theory. (b) Deprotonation of allyl bromide (Br-H). (c) Deprotonation of bromide ion (Br–H). **Notes:** In Fig. S2a, the horizontal axis represents the distance between the nitrogen and carbon atoms, both labeled in red. At an N-C distance of approximately 3 Å, the configuration corresponds to two NR_3 molecules and one allylic carbocation.

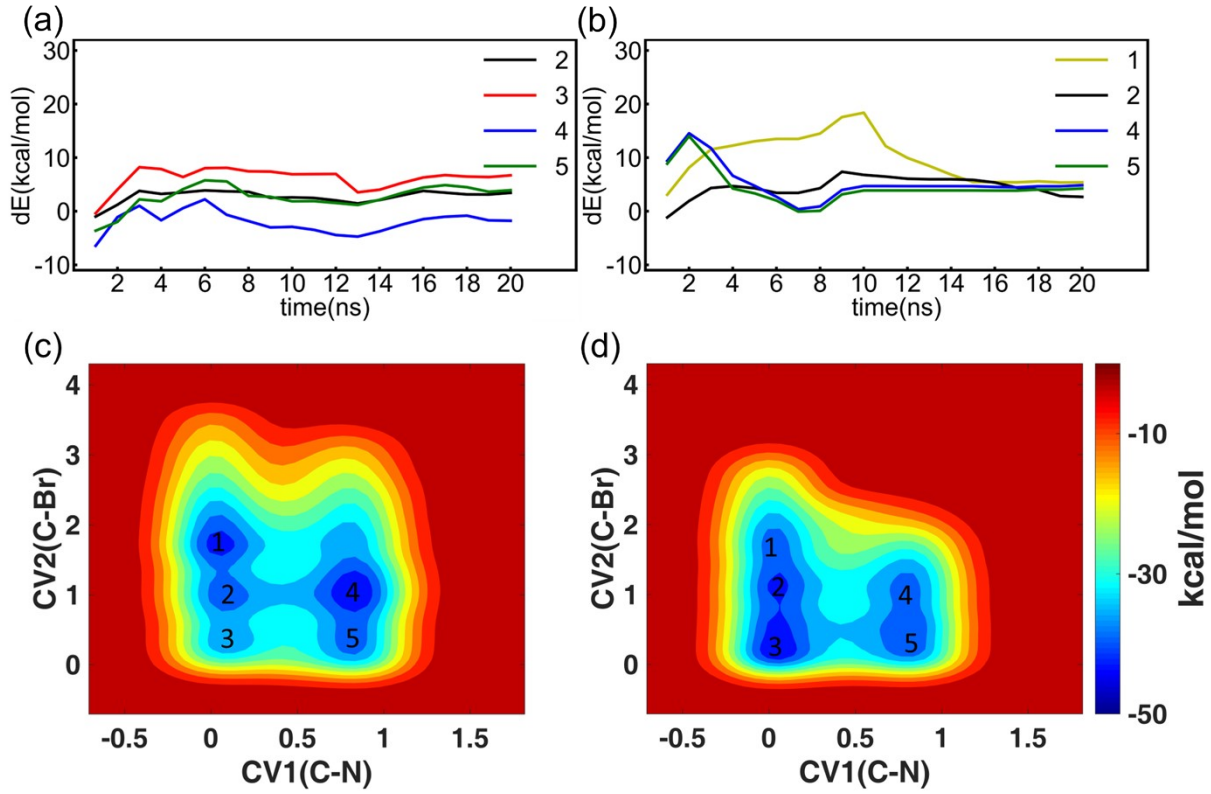

Fig. S3. Convergency of the free energy simulation with metadynamics for free energy profile shown in Fig. 2. (a) Free energy of the minimum states shown in (c) relative to the free energy of region 1; (b) Free energy of the minimum states shown in (d) relative to the free energy of region 3.

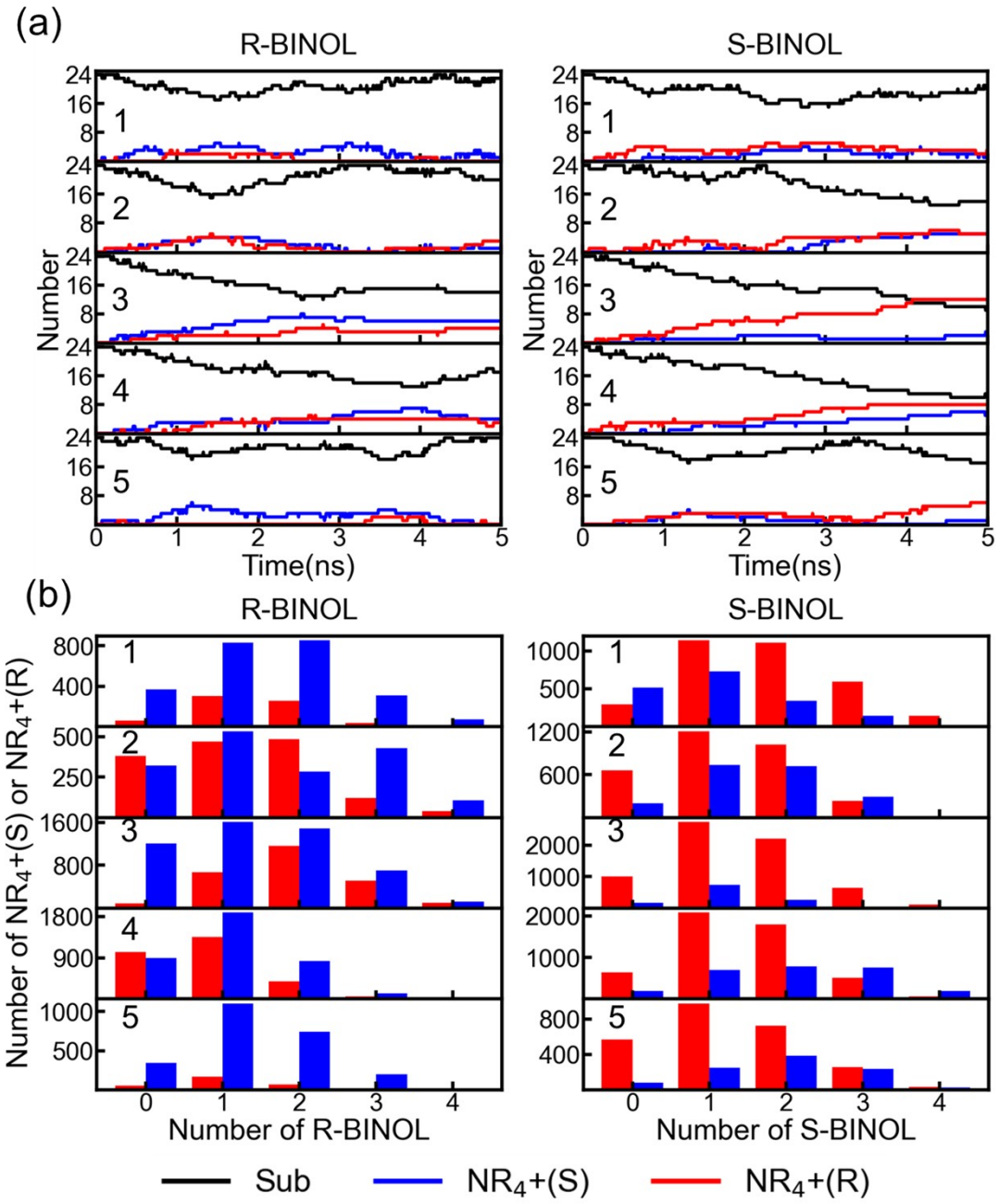

Fig. S4. (a) Five simulations catalyzed by R-BINOL and S-BINOL separately. The tracking plots of NR_3 (black), NR_4^+ (S) (blue) and NR_4^+ (R) (red). (b) Number of product molecules NR_4^+(S) (blue) and NR_4^+(R) (red) corresponding to the five simulations. **Notes:** The horizontal Axis represents the number of BINOL around the product molecule.

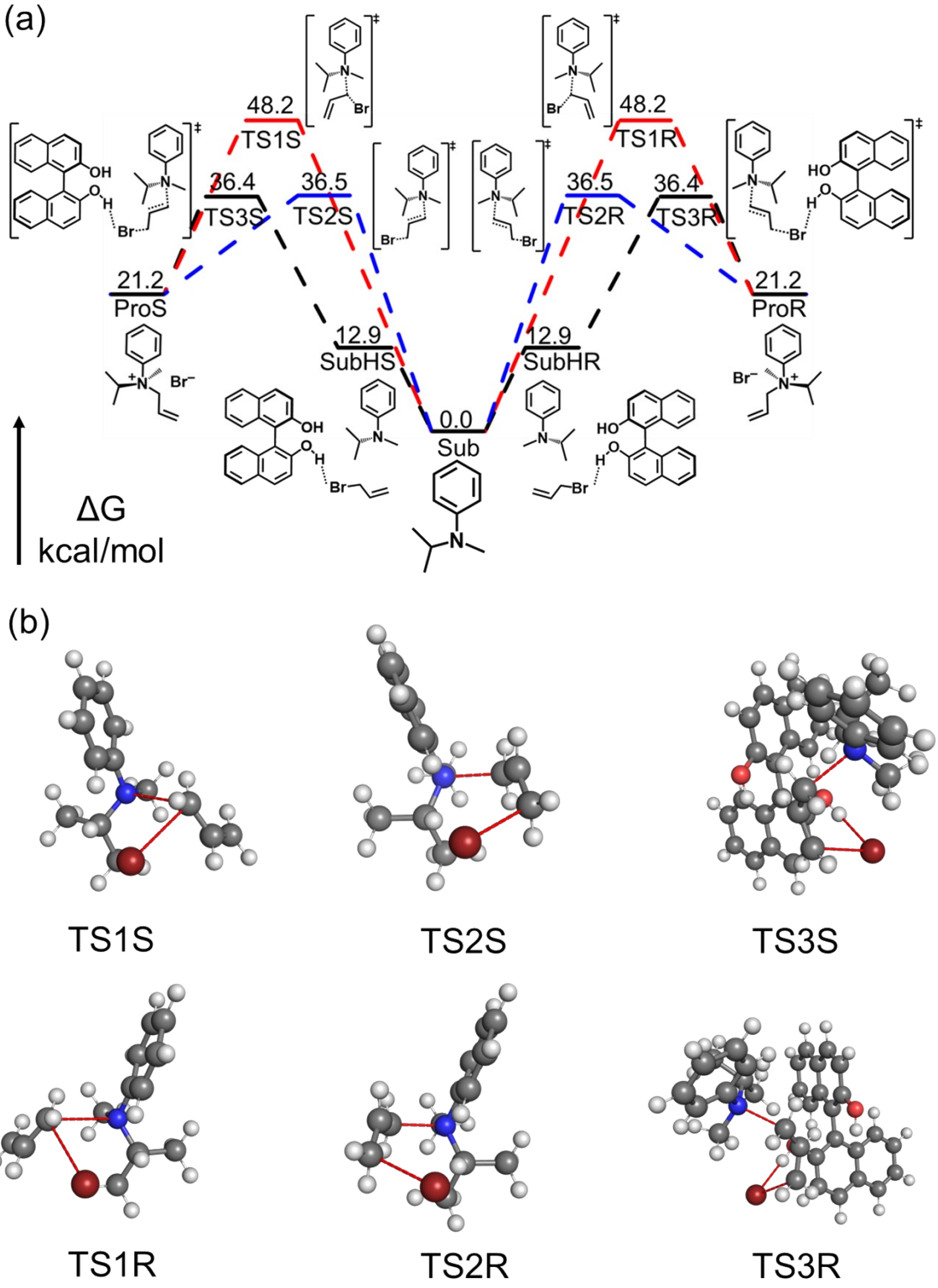

Fig. S5. (a) DFT calculations of the reaction pathways a-c (Fig. 1a-c) using the SMD model. (b) The 3D configurations of the corresponding transition states. The reaction pathways a-c shown in Fig. 1a, 1b and 1c are labeled in red, blue and black, respectively.

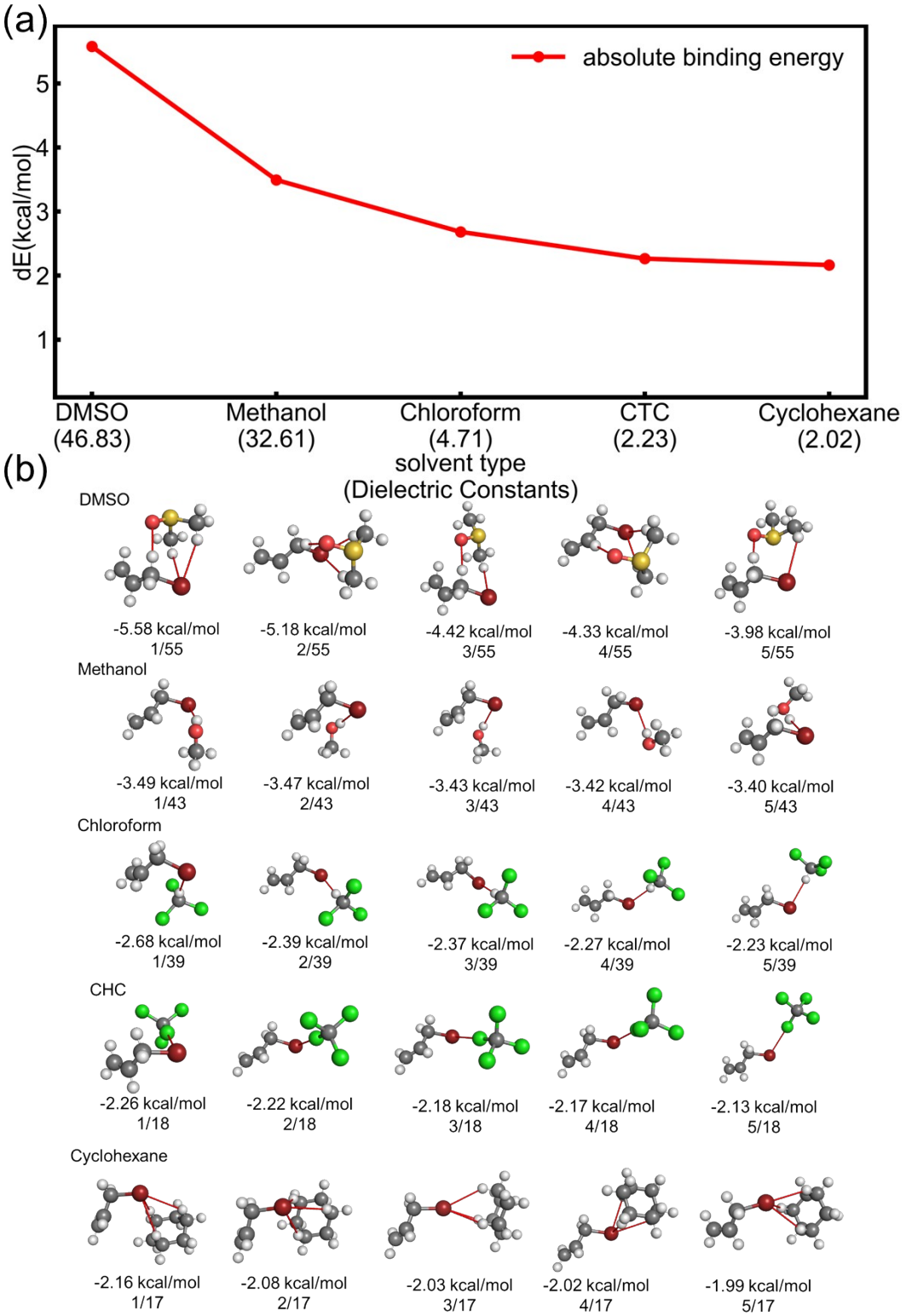

Fig. S6. (a) Absolute binding energies between allyl bromide and various solvent molecules. (b) Absolute binding energies of the five most stable binding structures for each solvent. **Notes:** Binding strengths are compared based on absolute energy values, with larger values indicating stronger interactions. The 100 binding structures are clustered into 55, 43, 39, 18, and 17 groups for DMSO, methanol, chloroform, CTC,

and cyclohexane, respectively.

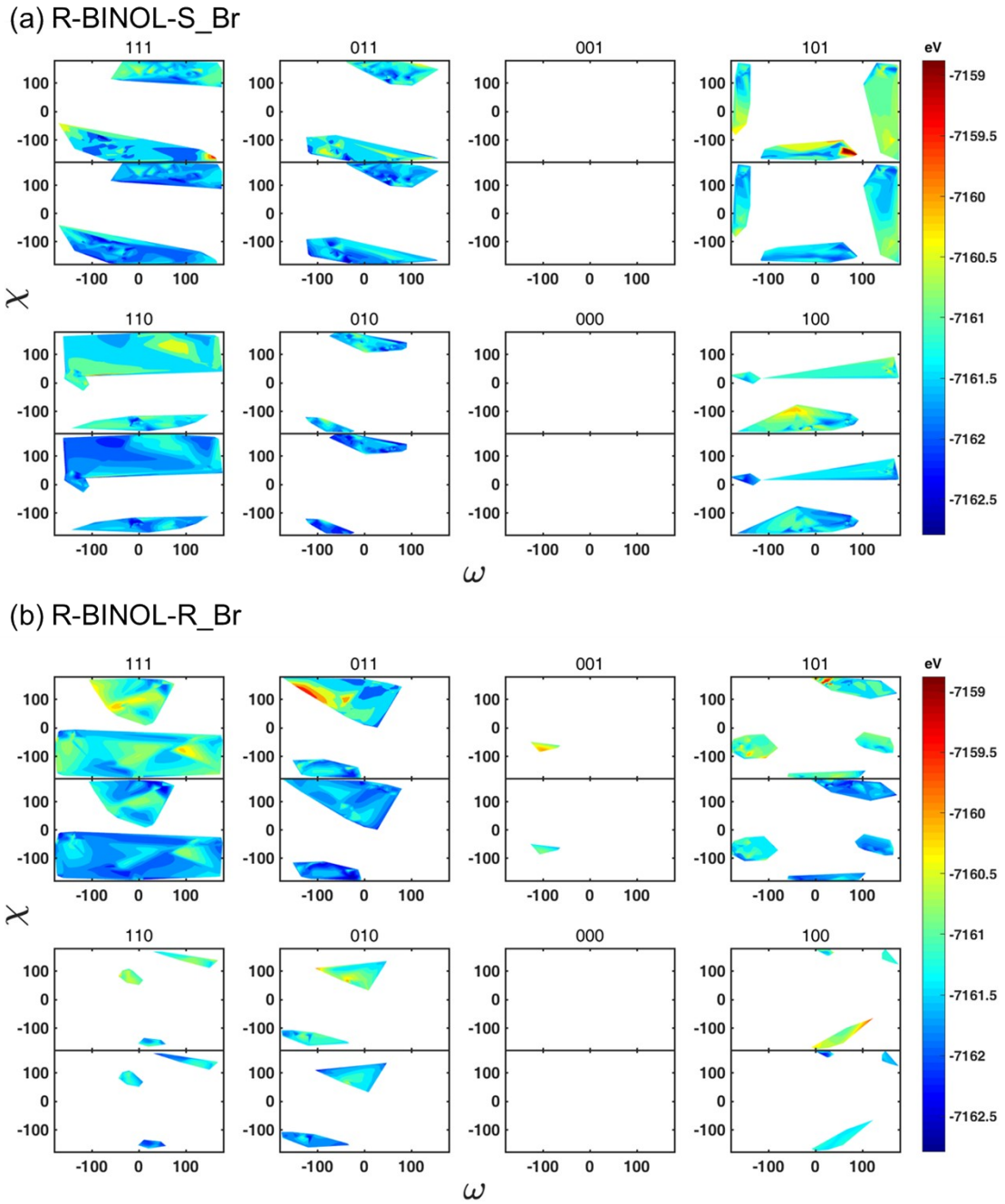

Fig. S7. Eenergy profiles for (a) R-BINOL-S_Br and (b) R-BINOL-R_Br at the PBE/DZVP-MOLOPT-SR-GTH level of theory (top) and with the DLP model (bottom).

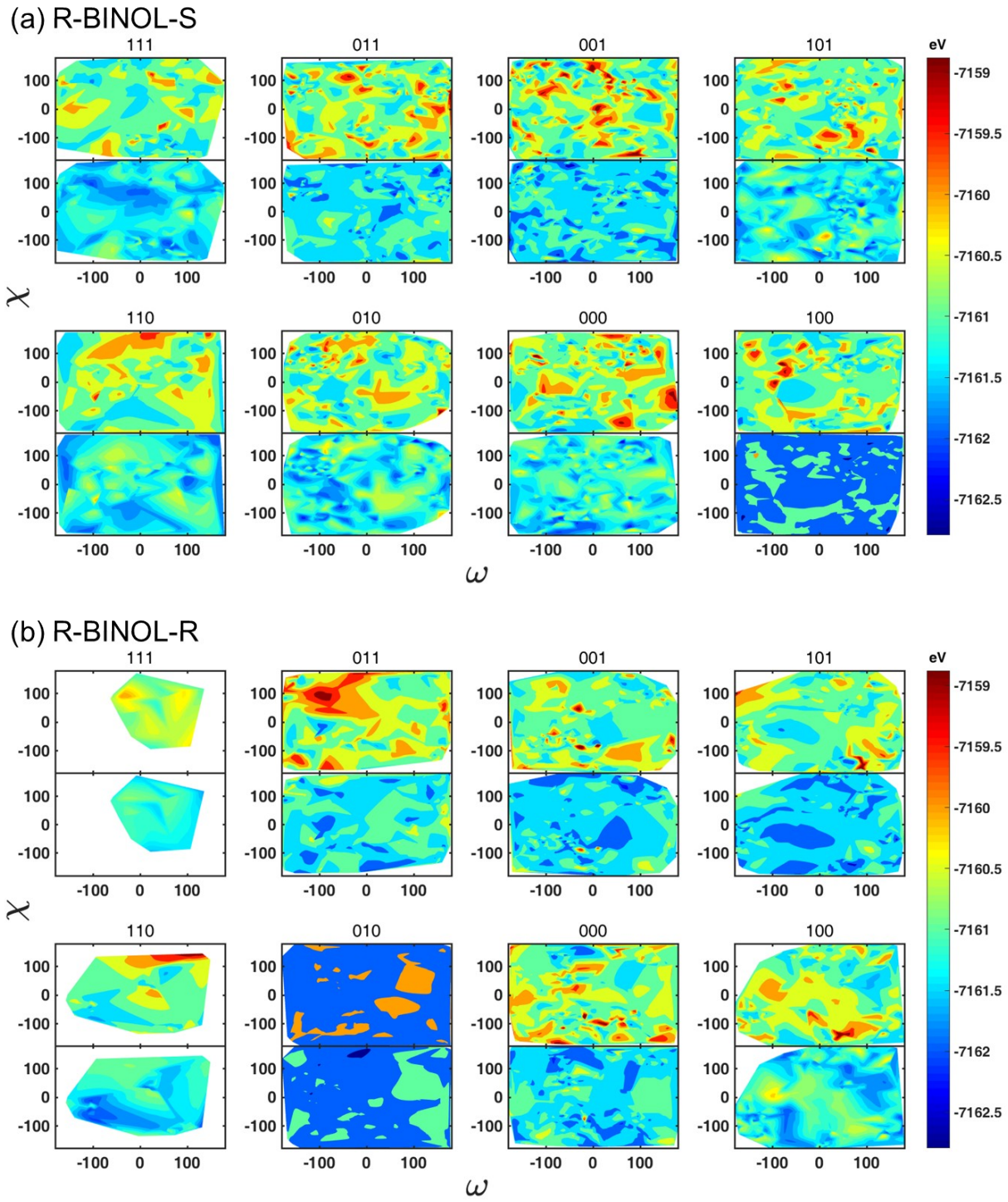

Fig. S8. Energy profiles for (a) R-BINOL-S and (b) R-BINOL-R at the PBE/DZVP-MOLOPT-SR-GTH level of theory (top) and with the DLP model (bottom).

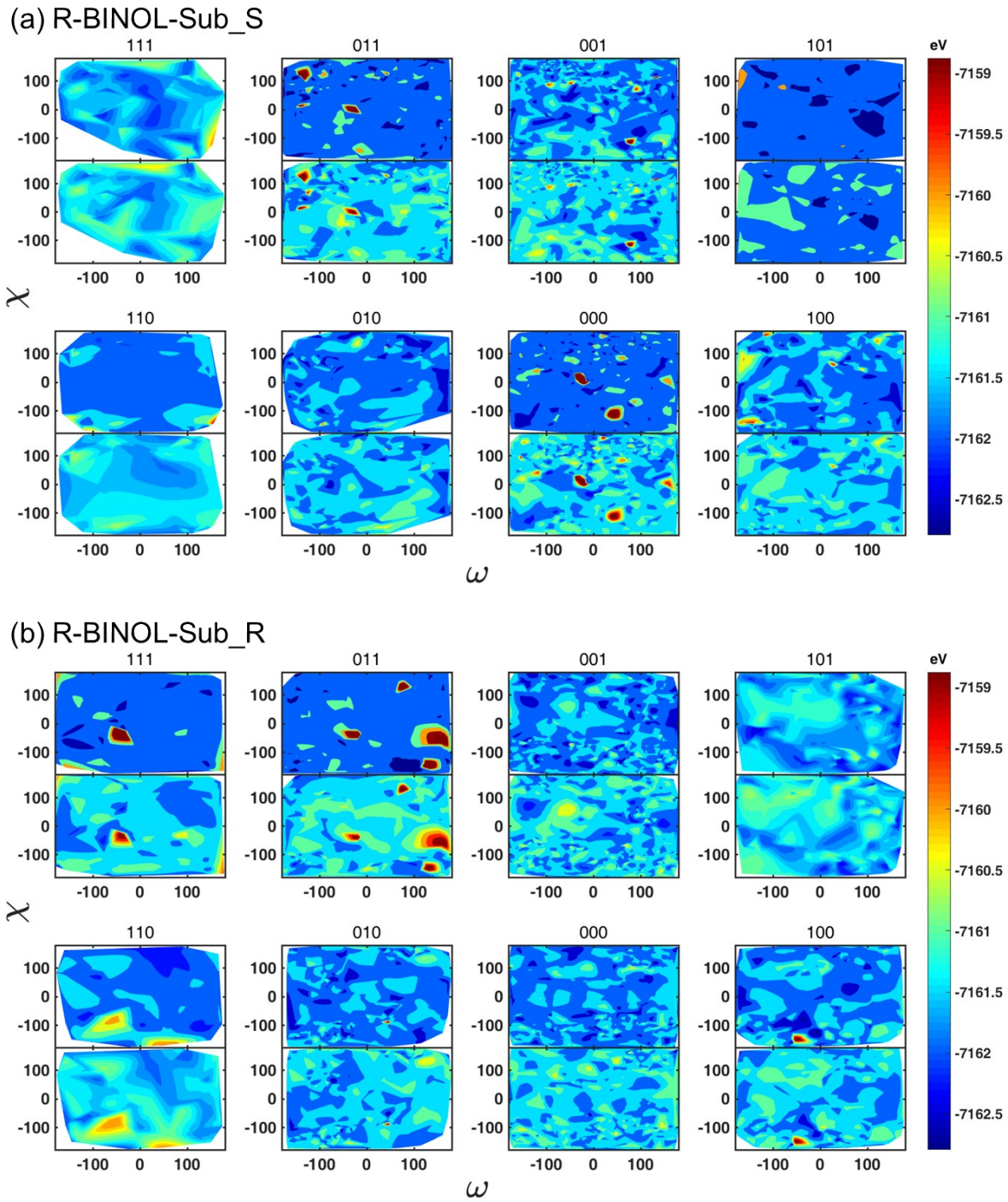

Fig. S9. Energy profiles for (a) R-BINOL-Sub_S and (b) R-BINOL-Sub_R at the PBE/DZVP-MOLOPT-SR-GTH level of theory (top) and with the DLP model (bottom).

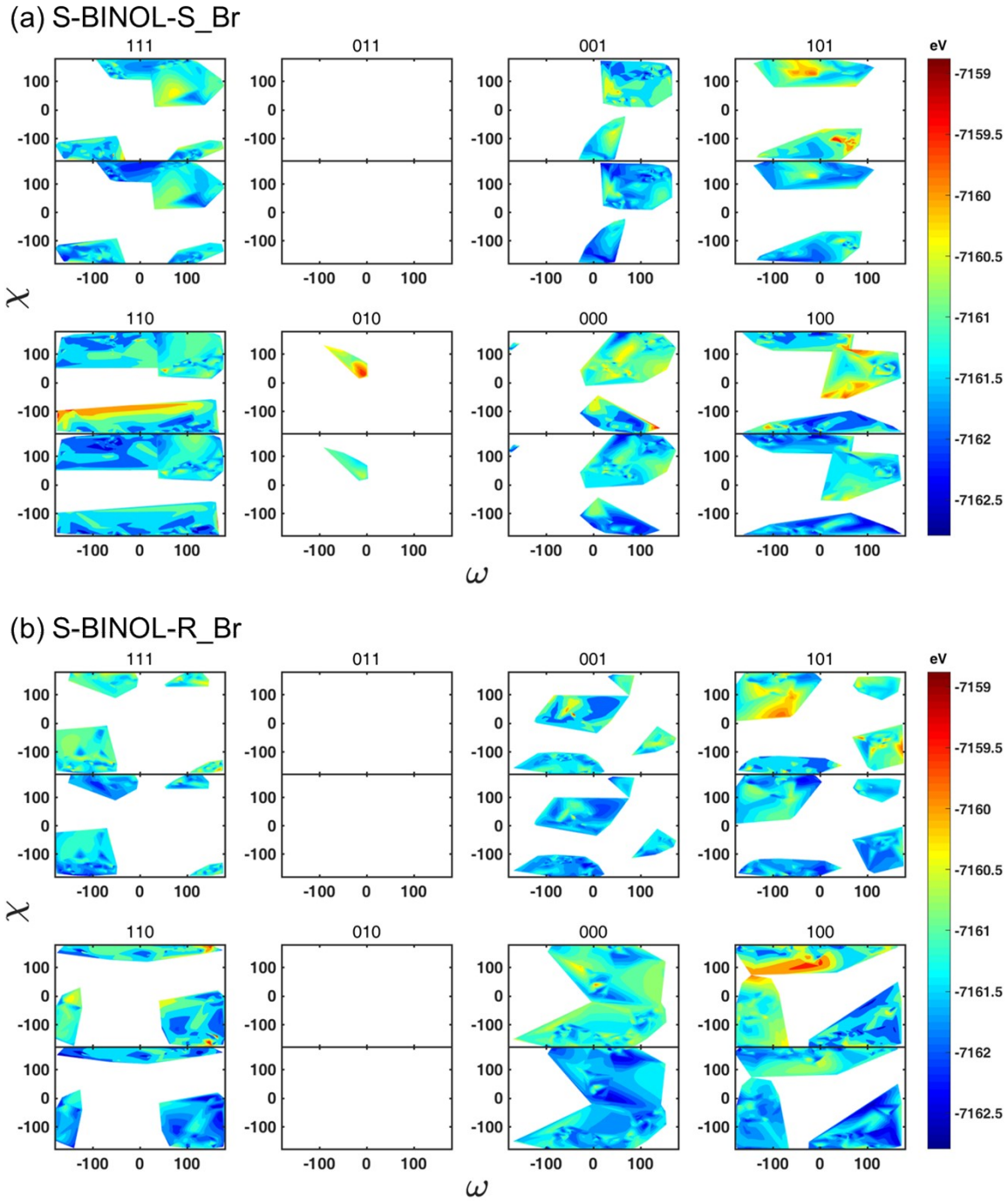

Fig. S10. Energy profiles for (a) S-BINOL-S_Br and (b) S-BINOL-R_Br at the PBE/DZVP-MOLOPT-SR-GTH level of theory (top) and with the DLP model (bottom).

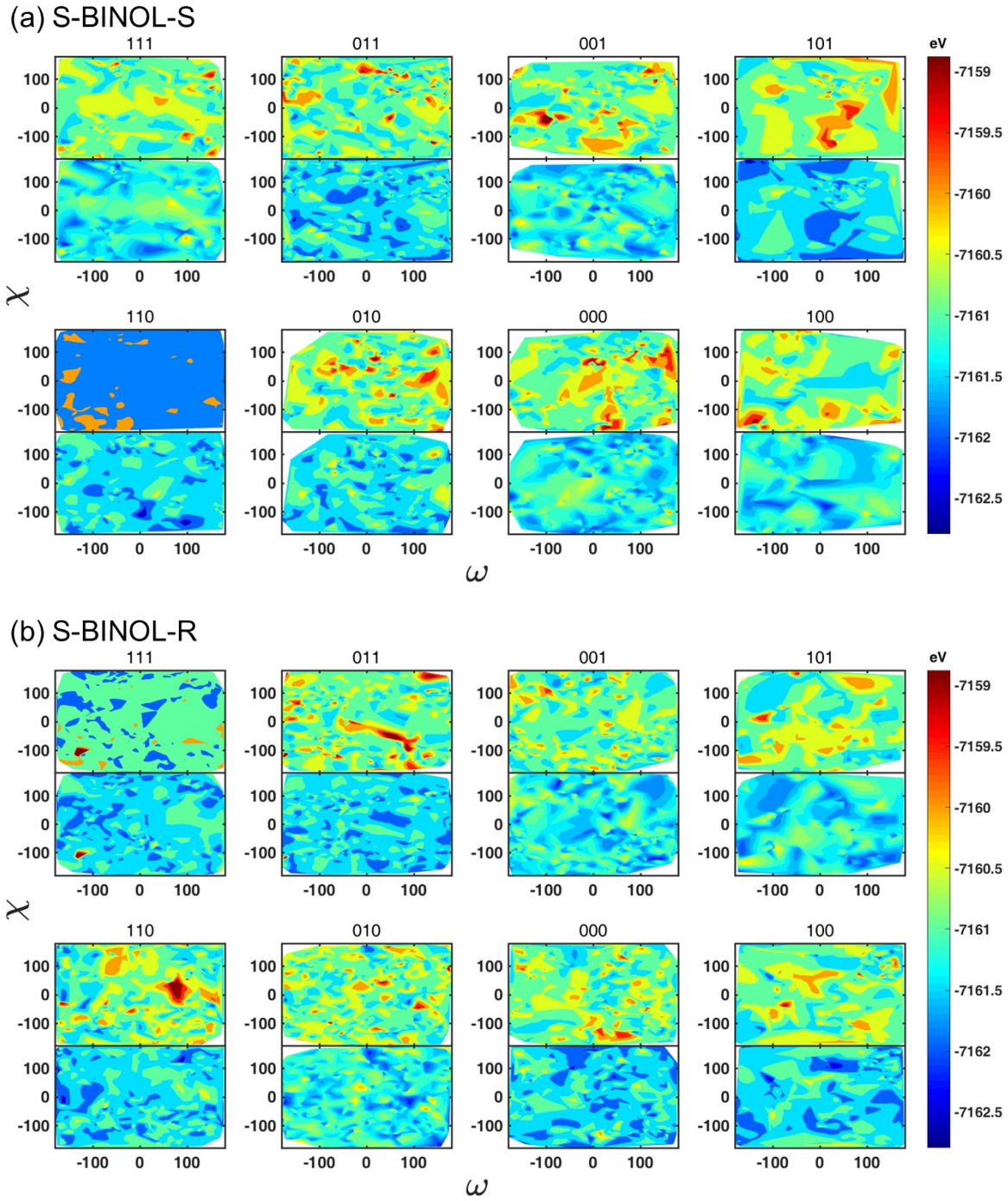

Fig. S11. Energy profiles for (a) S-BINOL-S and (b) S-BINOL-R at the PBE/DZVP-MOLOPT-SR-GTH level of theory (top) and with the DLP model (bottom).

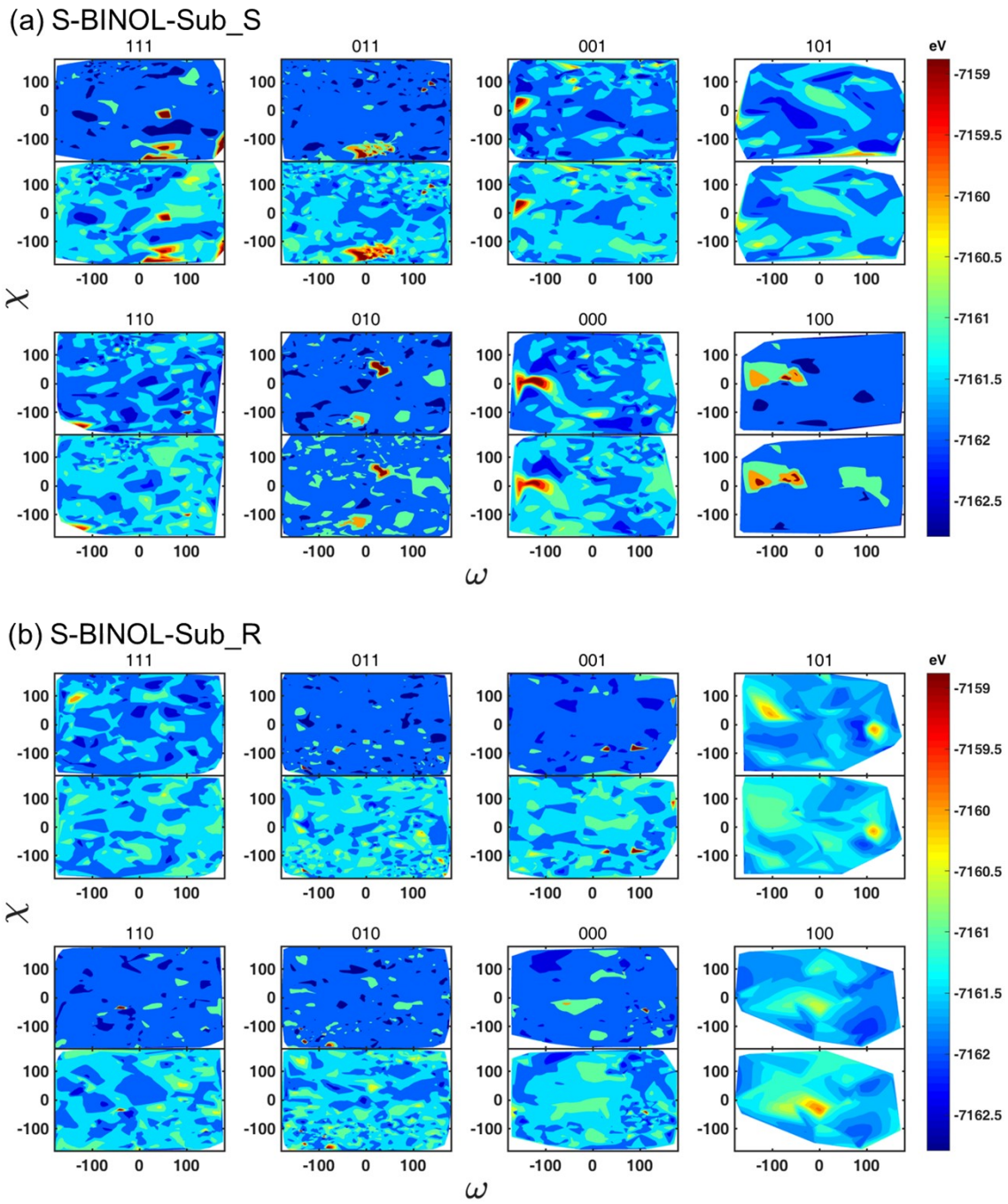

Fig. S12. Energy profiles for (a) S-BINOL-Sub_S and (b) S-BINOL-Sub_R at the PBE/DZVP-MOLOPT-SR-GTH level of theory (top) and with the DLP model (bottom).

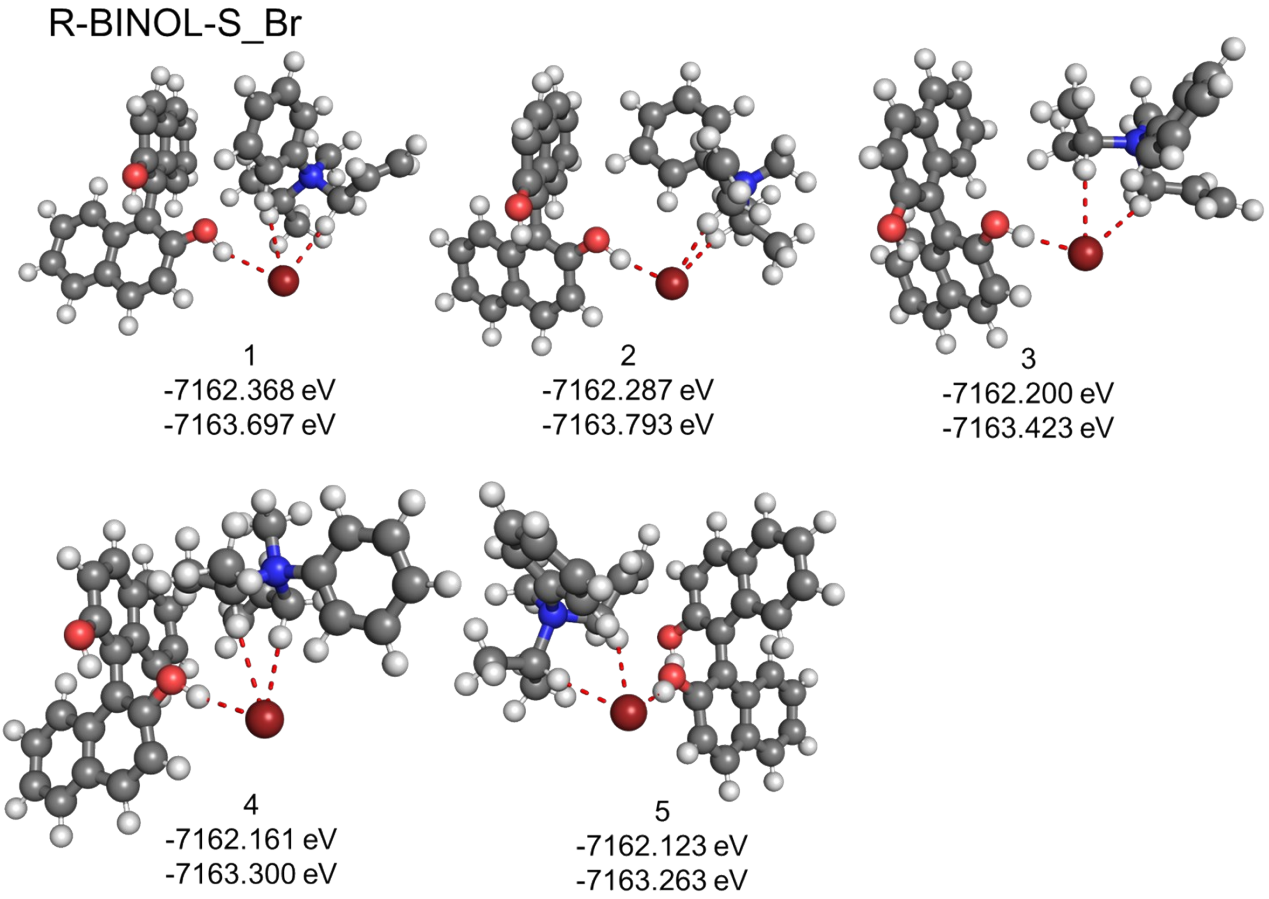

Fig. S13. The structures and energies at the PBE/DZVP-MOLOPT-SR-GTH level of theory (top) and with the DLP model (bottom) for R-BINOL-S_Br. **Notes:** These structures are sorted according to their DFT energies.

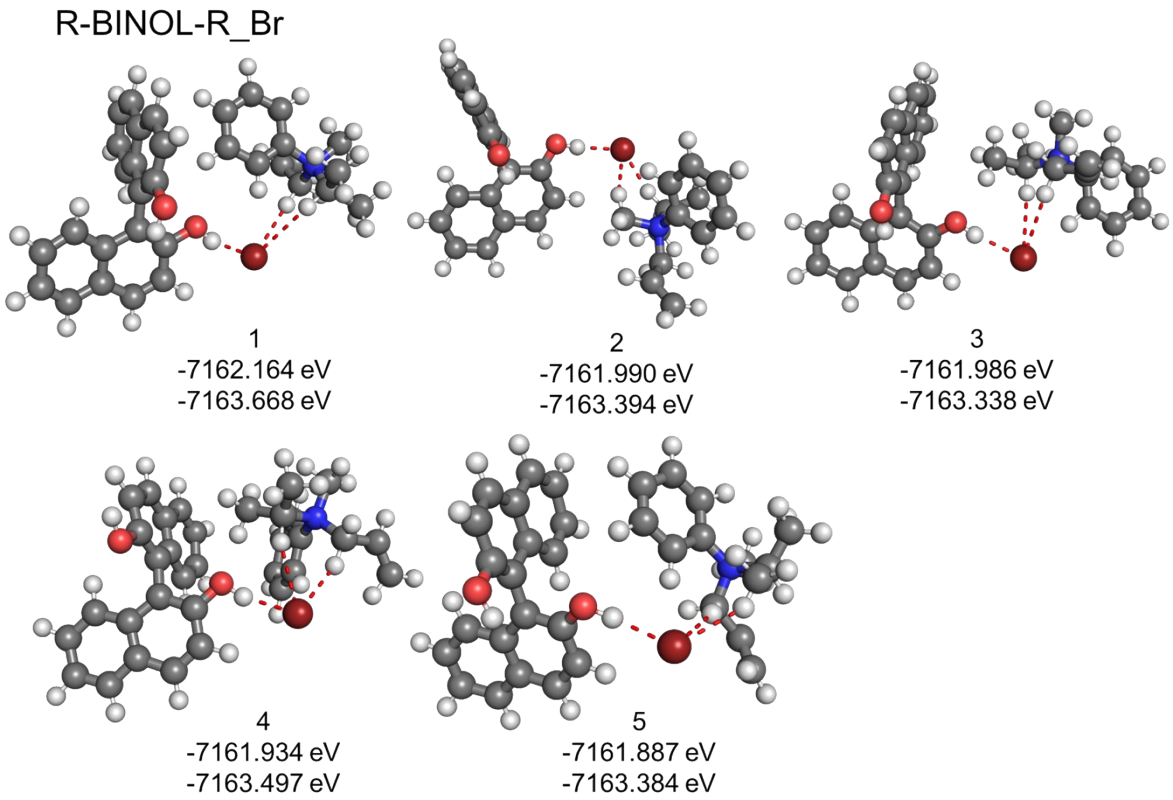

Fig. S14. The structures and energies at the PBE/DZVP-MOLOPT-SR-GTH level of theory (top) and with the DLP model (bottom) for R-BINOL-R_Br. **Notes:** These structures are sorted according to their DFT energies.

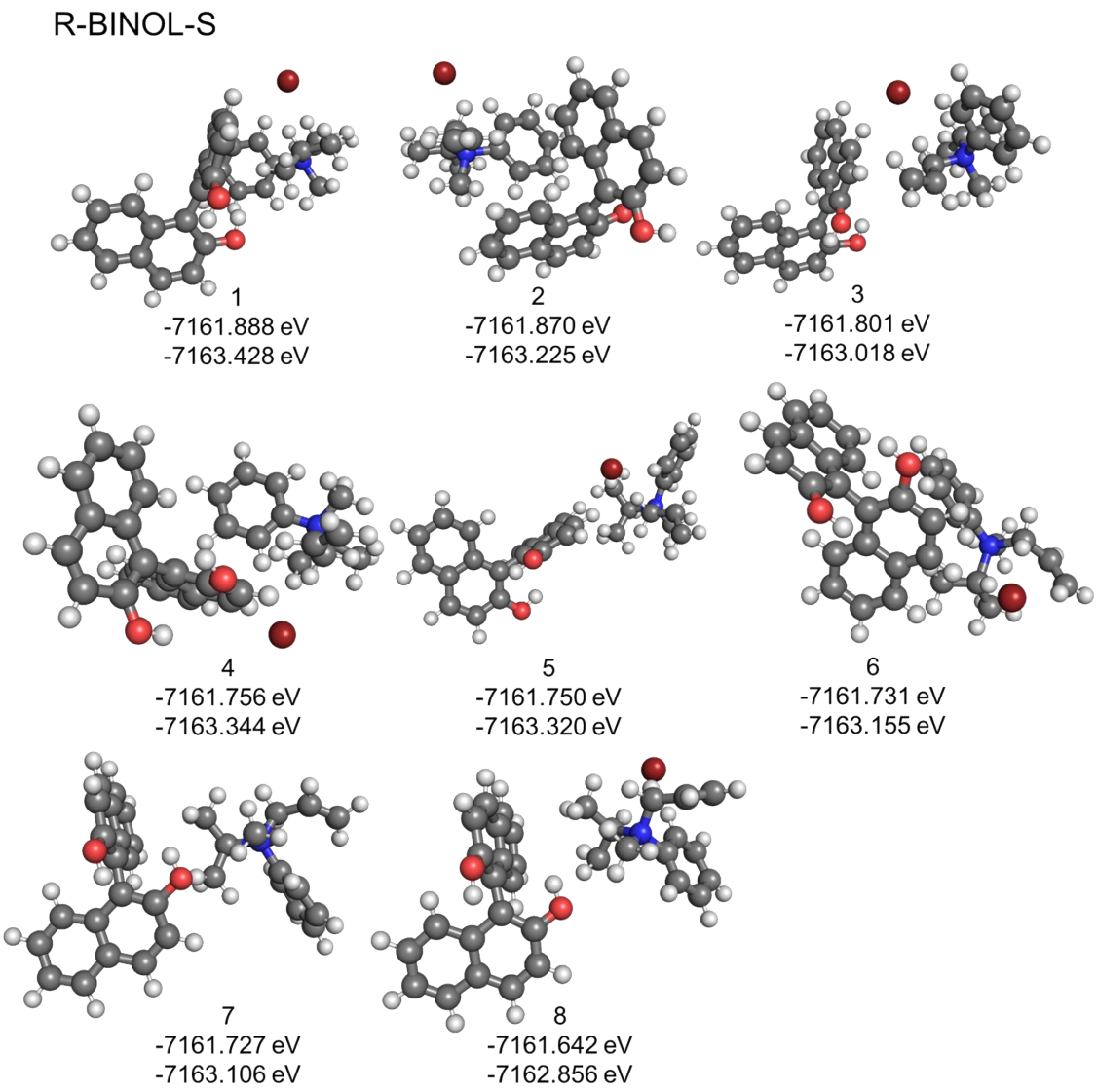

Fig. S15. The structures and energies at the PBE/DZVP-MOLOPT-SR-GTH level of theory (top) and with the DLP model (bottom) for R-BINOL-S. **Notes:** These structures are sorted according to their DFT energies.

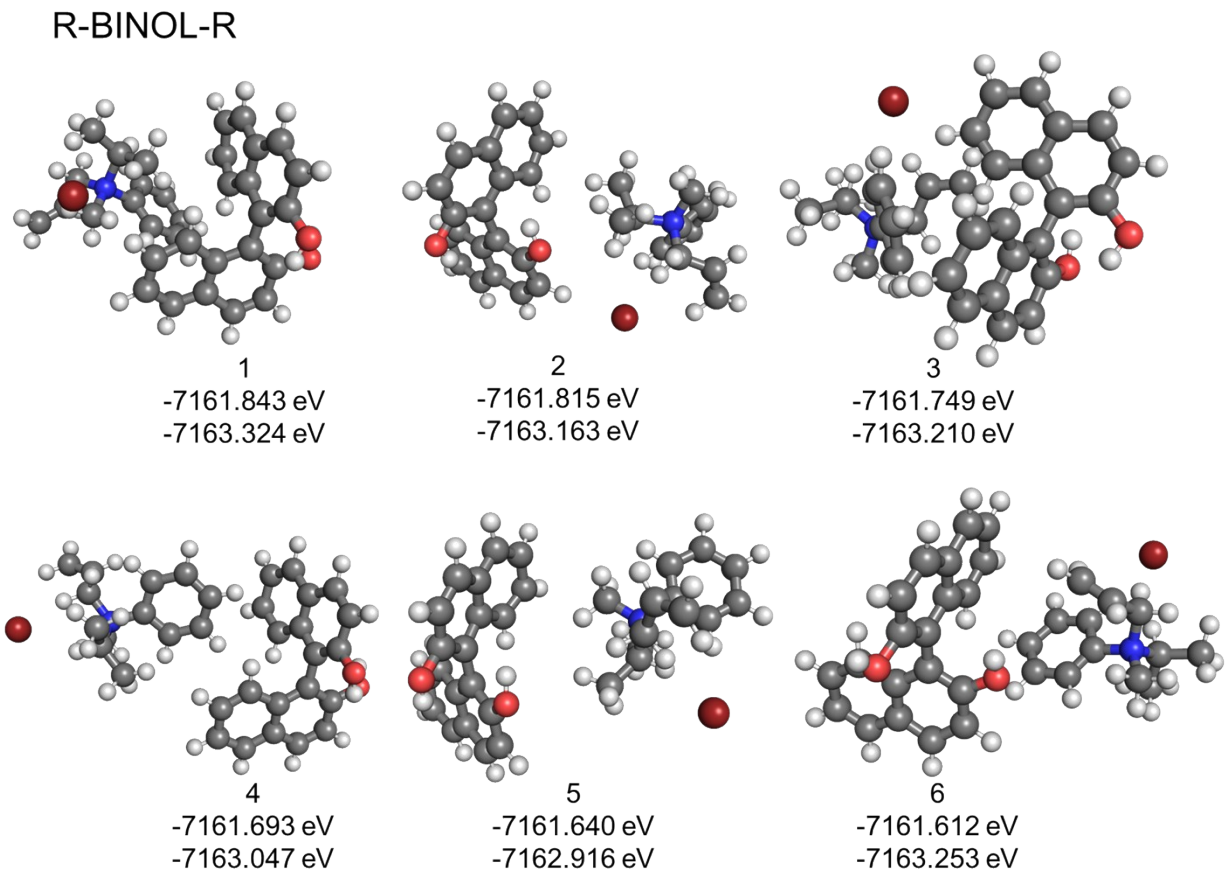

Fig. S16. The structures and energies at the PBE/DZVP-MOLOPT-SR-GTH level of theory (top) and with the DLP model (bottom) for R-BINOL-R. **Notes:** These structures are sorted according to their DFT energies.

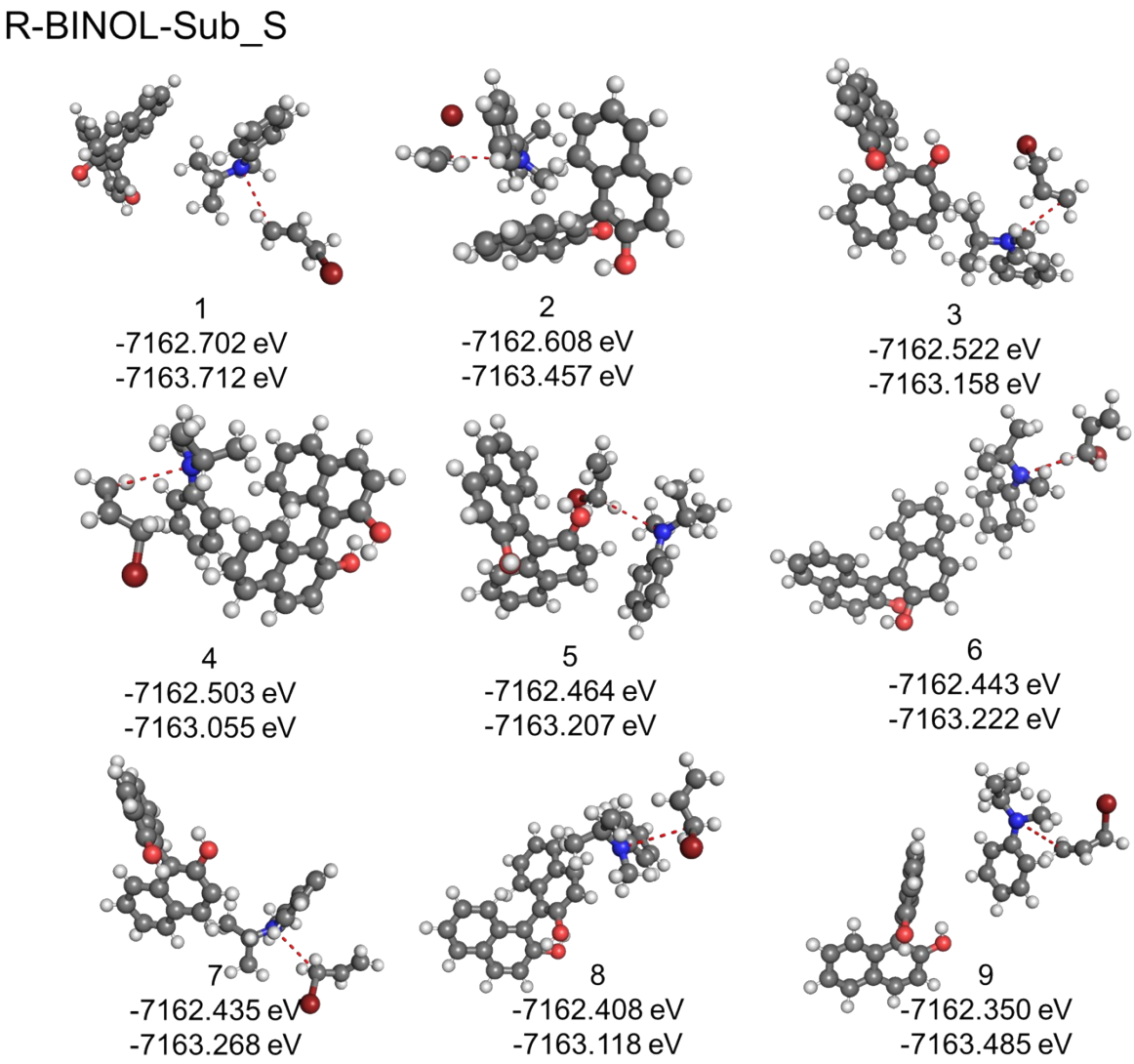

Fig. S17. The structures and energies at the PBE/DZVP-MOLOPT-SR-GTH level of theory (top) and with the DLP model (bottom) for R-BINOL-Sub_S. **Notes:** These structures are sorted according to their DFT energies.

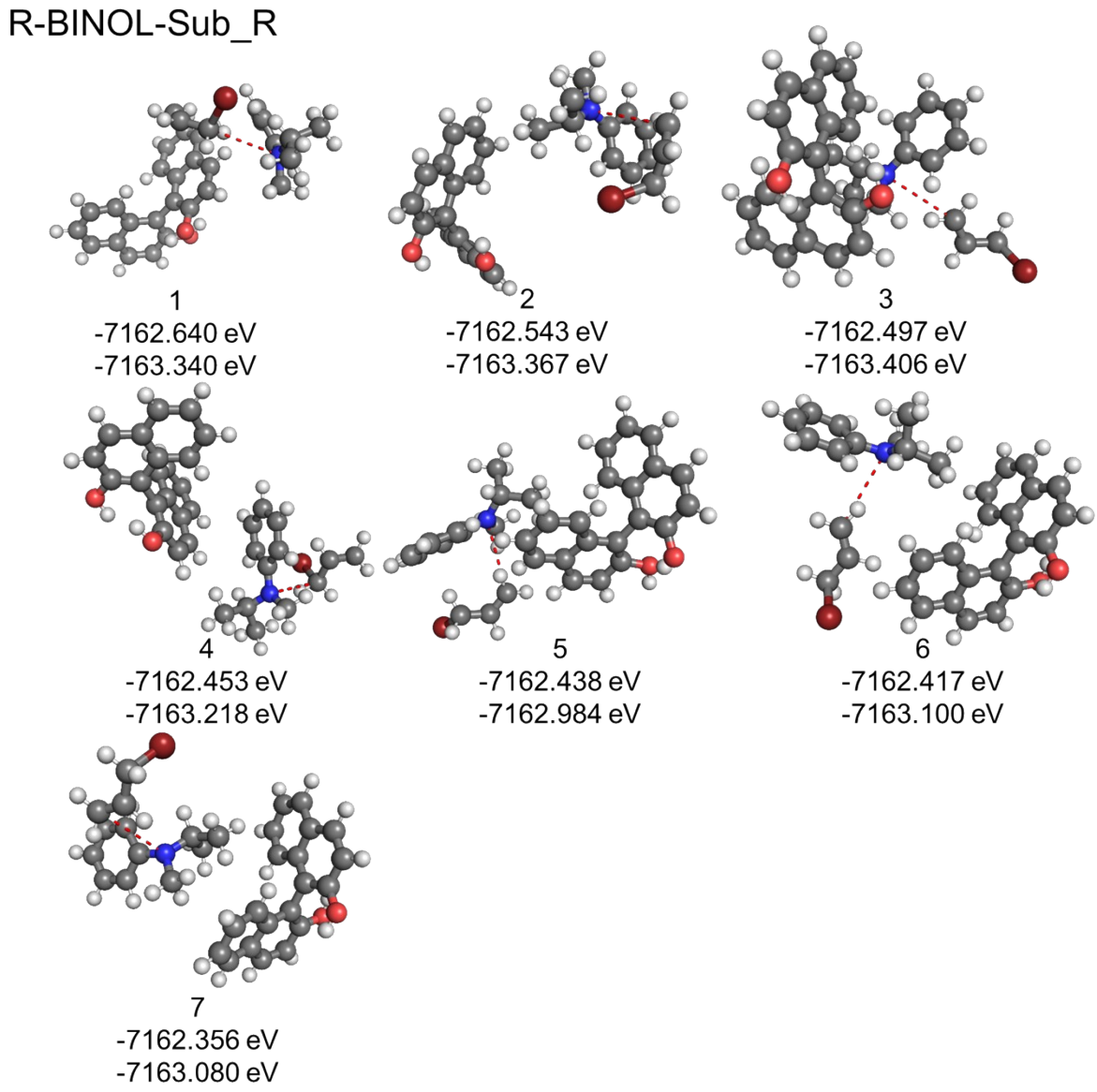

Fig. S18. The structures and energies at the PBE/DZVP-MOLOPT-SR-GTH level of theory (top) and with the DLP model (bottom) for R-BINOL-Sub_R. **Notes:** These structures are sorted according to their DFT energies.

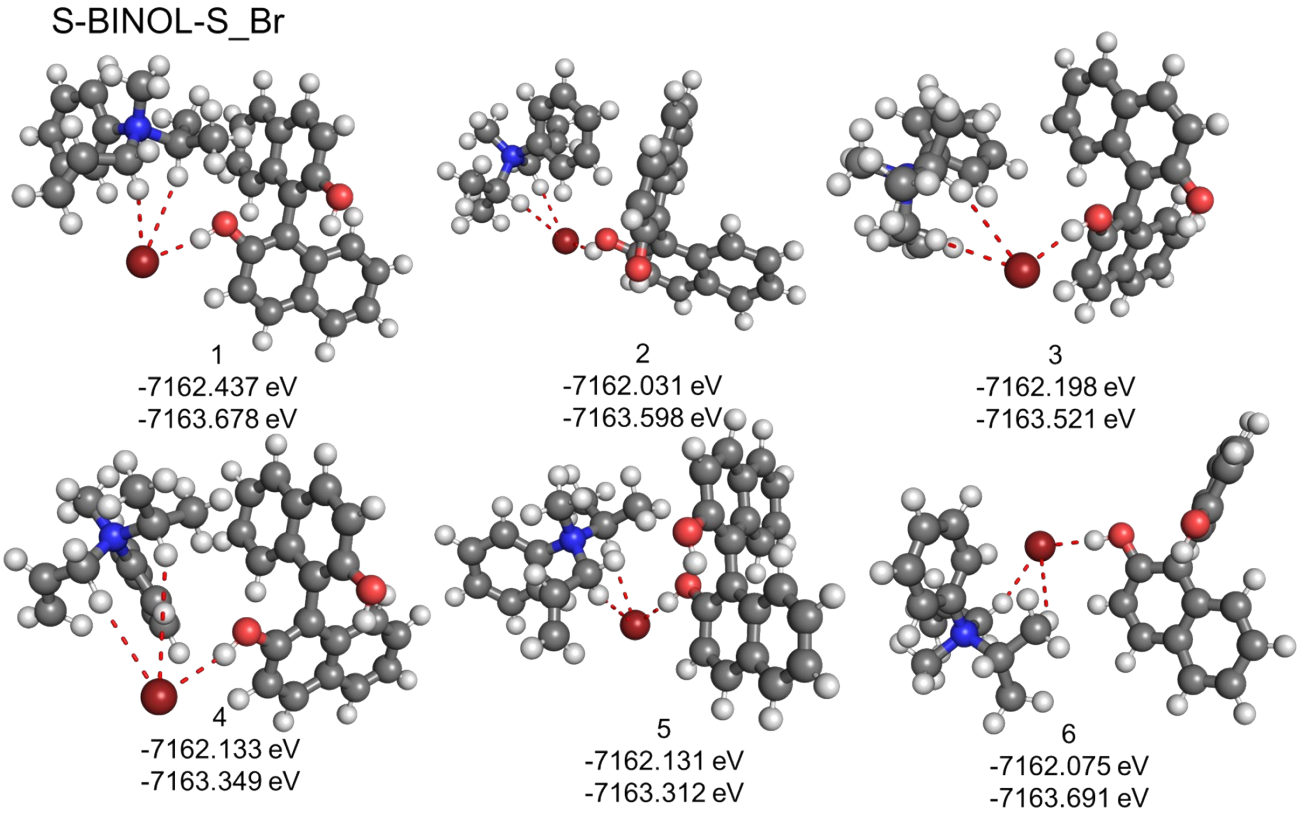

Fig. S19. The structures and energies at the PBE/DZVP-MOLOPT-SR-GTH level of theory (top) and with the DLP model (bottom) for S-BINOL-S_Br. **Notes:** These structures are sorted according to their DFT energies.

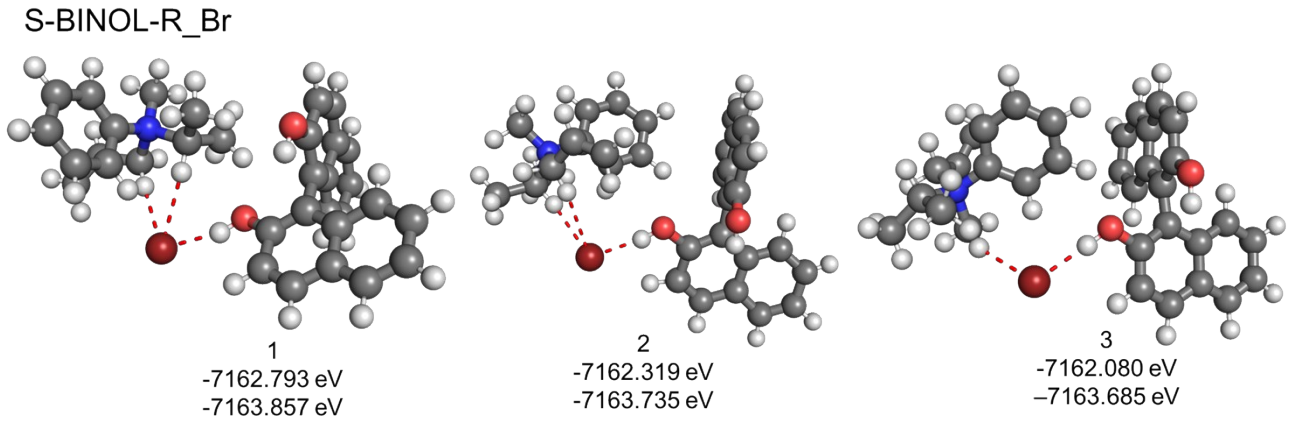

Fig. S20. The structures and energies at the PBE/DZVP-MOLOPT-SR-GTH level of theory (top) and with the DLP model (bottom) for S-BINOL-R_Br. **Notes:** These structures are sorted according to their DFT energies.

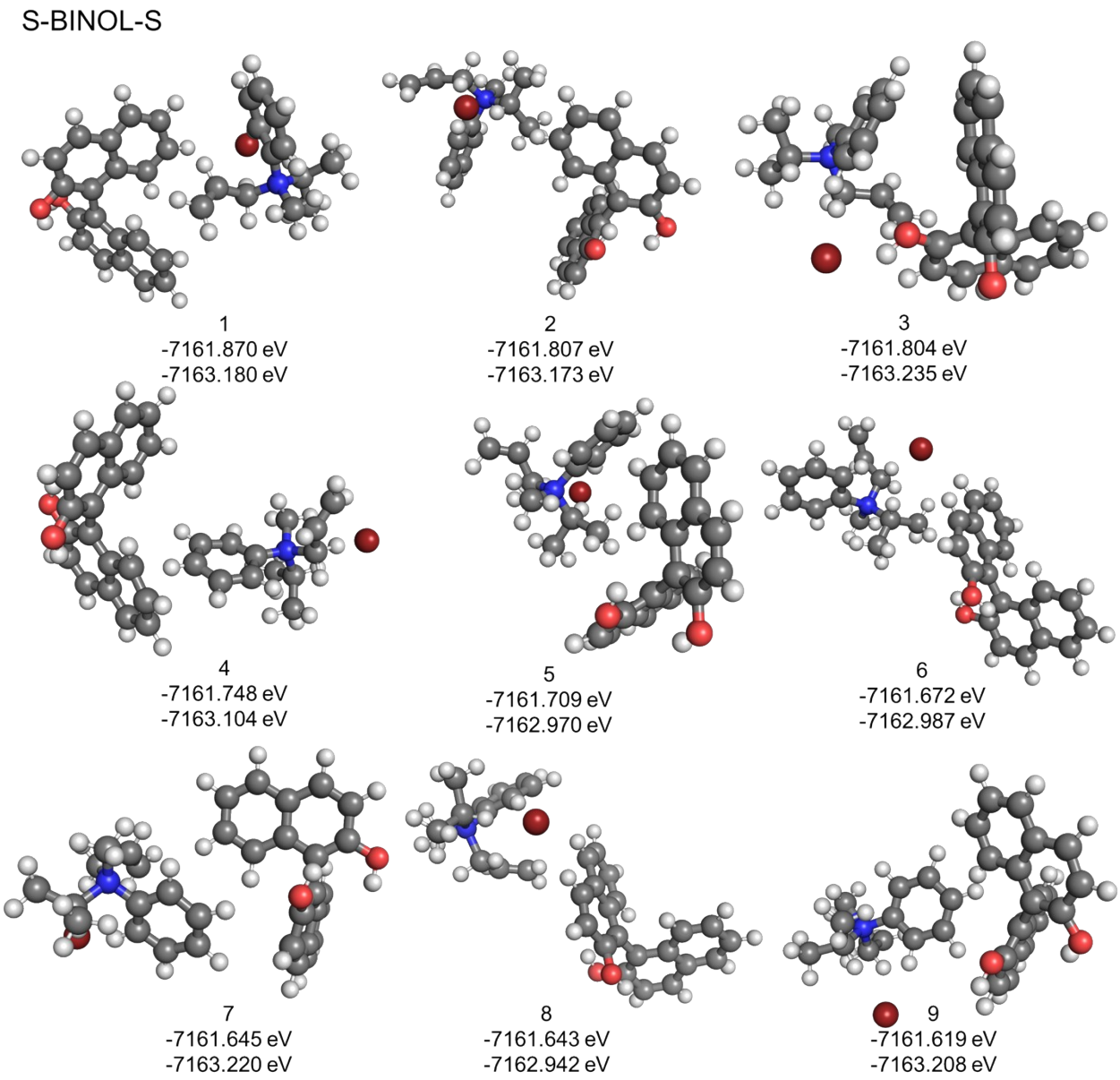

Fig. S21. The structures and energies at the PBE/DZVP-MOLOPT-SR-GTH level of theory (top) and with the DLP model (bottom) for S-BINOL-S. **Notes:** These structures are sorted according to their DFT energies.

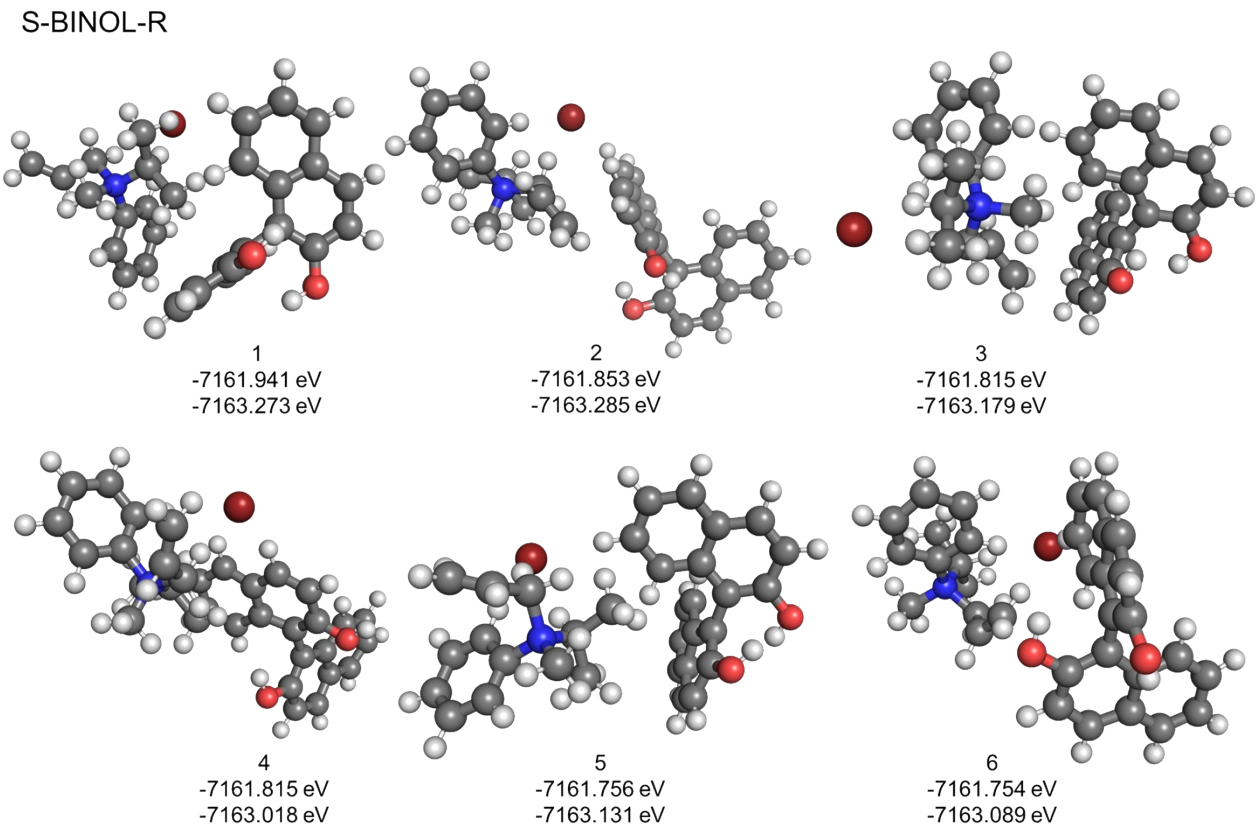

Fig. S22. The structures and energies at the PBE/DZVP-MOLOPT-SR-GTH level of theory (top) and with the DLP model (bottom) for S-BINOL-R. **Notes:** These structures are sorted according to their DFT energies.

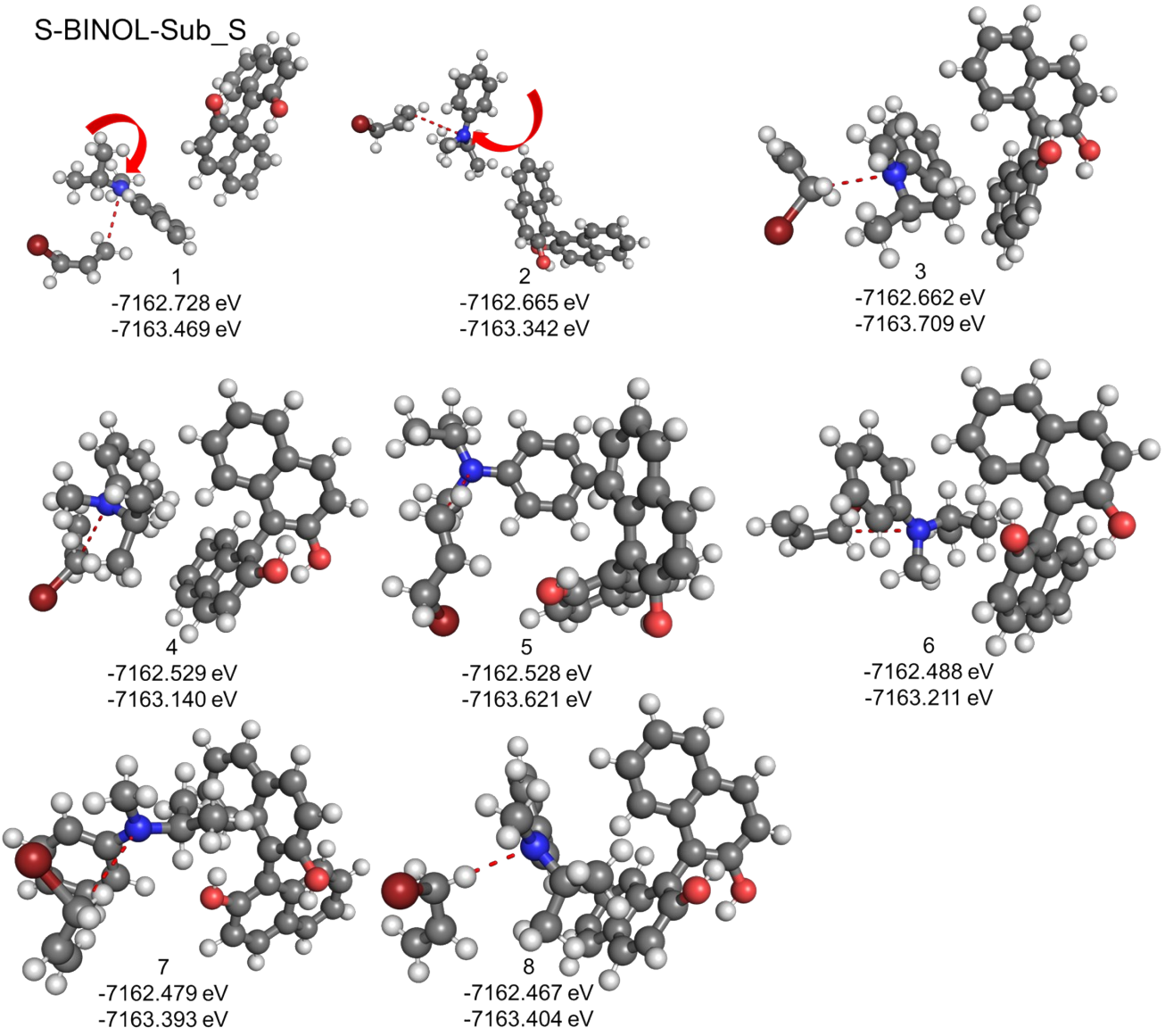

Fig. S23. The structures and energies at the PBE/DZVP-MOLOPT-SR-GTH level of theory (top) and with the DLP model (bottom) for S-BINOL-Sub_S. **Notes:** These structures are sorted according to their DFT energies.

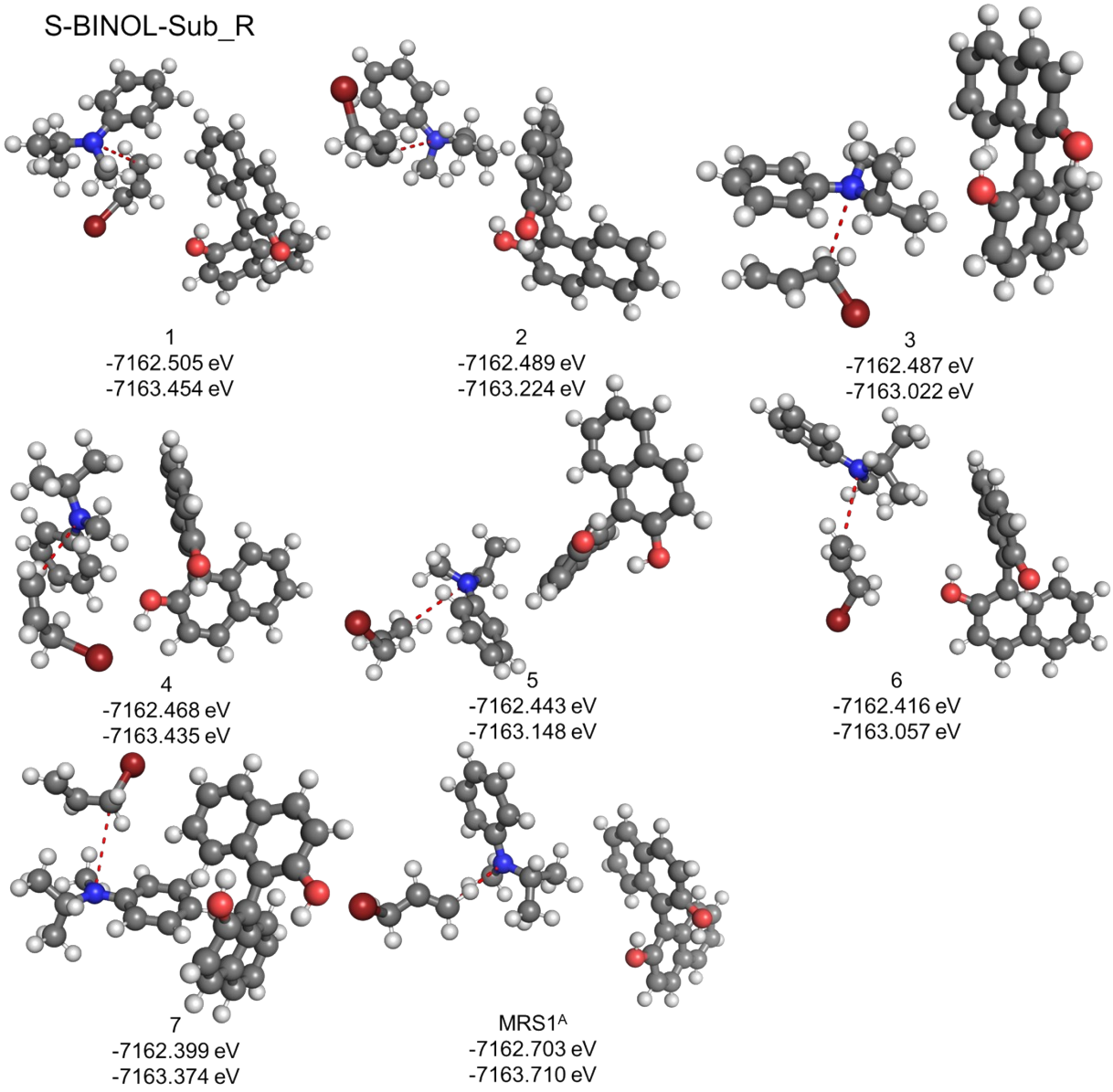

Fig. S24. The structures and energies at the PBE/DZVP-MOLOPT-SR-GTH level of theory (top) and with the DLP model (bottom) for S-BINOL-Sub_R. **Notes:** These structures are sorted according to their DFT energies. A. S-BINOL-Sub_R(MRS1) represents the mirror image of R-BINOL-Sub_S(1) in Fig. S17.

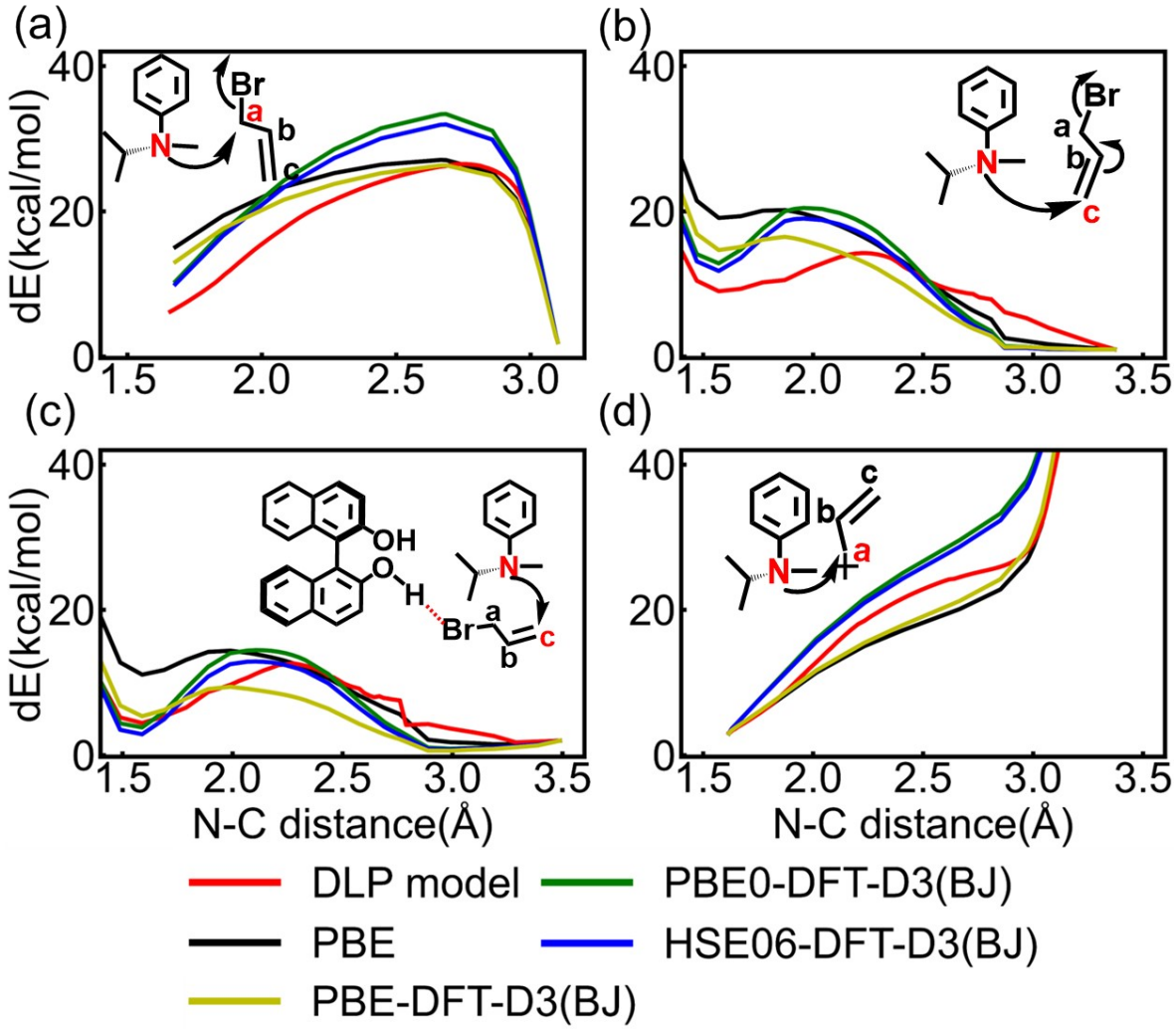

Fig. S25. Energetics along the N-C distances calculated using the DLP model and different DFT methods for $NR_4^+(S)$ structures. (a-d): Reaction coordinate diagrams corresponding to the reaction pathways a-d (Fig. 1a-d), respectively. **Notes:** In Fig. S25a-d, the horizontal axis represents the distance between the nitrogen and carbon atoms, both labeled in red.

References

1. M. J. Frisch, G. W. Trucks, H. B. Schlegel, G. E. Scuseria, M. A. Robb, J. R. Cheeseman, G. Scalmani, V. Barone, G. A. Petersson, H. Nakatsuji, X. Li, M. Caricato, A. V. Marenich, J. Bloino, B. G. Janesko, R. Gomperts, B. Mennucci, H. P. Hratchian, J. V. Ortiz, A. F. Izmaylov, J. L. Sonnenberg, D. F. Williams, F. Lipparini, F. Egidi, J. Goings, B. Peng, A. Petrone, T. Henderson, D. Ranasinghe, V. G. Zakrzewski, J. Gao, N. Rega, G. Zheng, W. Liang, M. Hada, M. Ehara, K. Toyota, R. Fukuda, J. Hasegawa, M. Ishida, T. Nakajima, Y. Honda, O. Kitao, H. Nakai, T. Vreven, K. Throssell, J. A. Montgomery, J. E. Peralta, F. Ogliaro, M. J. Bearpark, J. J. Heyd, E. N. Brothers, K. N. Kudin, V. N. Staroverov, T. A. Keith, R. Kobayashi, J. Normand, K. Raghavachari, A. P. Rendell, J. C. Burant, S. S. Iyengar, J. Tomasi, M. Cossi, J. M. Millam, M. Klene, C. Adamo, R. Cammi, J. W. Ochterski, R. L. Martin, K. Morokuma, O. Farkas, J. B. Foresman and D. J. Fox, *Gaussian 16, Revision A.03, Gaussian Inc, Wallingford CT, 2016*.
2. K. Raghavachari, *Theor. Chem. Acc.*, 2000, **103**, 361-363.
3. W. J. Hehre, R. Ditchfield and J. A. Pople, *J. Chem. Phys.*, 1972, **56**, 2257-2261.
4. M. M. Francl, W. J. Pietro, W. J. Hehre, J. S. Binkley, M. S. Gordon, D. J. Defrees and J. A. Pople, *J. Chem. Phys.*, 1982, **77**, 3654-3665.
5. A. V. Marenich, C. J. Cramer and D. G. Truhlar, *J. Phys. Chem. B*, 2009, **113**, 6378-6396.
6. M. P. Walsh, J. M. Phelps, M. E. Lennon, D. S. Yufit and M. O. Kitching, *Nature*, 2021, **597**, 70-76.
7. L. Bai, J. Y. Liang and C. Y. Dang, *Knowl-Based Syst.*, 2011, **24**, 785-795.
8. Arthur D and V. S., New Orleans, LA, 2007.
9. A. Lee, J. H. Yang, J. H. Oh, B. P. Hay, K. Lee, V. M. Lynch, J. L. Sessler and S. K. Kim, *Chem. Sci.*, 2023, **14**, 1218-1226.
10. W. H. Duan, Q. Wang and F. Collins, *Chem. Sci.*, 2011, **2**, 1407-1413.
11. P. Çarçabal, E. J. Cocinero and J. P. Simons, *Chem. Sci.*, 2013, **4**, 1830-1836.
12. T. D. Kühne, M. Iannuzzi, M. Del Ben, V. V. Rybkin, P. Seewald, F. Stein, T. Laino, R. Z. Khaliullin, O. Schütt, F. Schiffmann, D. Golze, J. Wilhelm, S. Chulkov, M. H. Bani-Hashemian, V. Weber, U. Borstnik, M. Taillefumier, A. S. Jakobovits, A. Lazzaro, H. Pabst, T. Müller, R. Schade, M. Guidon, S. Andermatt, N. Holmberg, G. K. Schenter, A. Hehn, A. Bussy, F. Belleflamme, G. Tabacchi, A. Glöss, M. Lass, I. Bethune, C. J. Mundy, C. Plessl, M. Watkins, J. VandeVondele, M. Krack and J. Hutter, *J. Chem. Phys.*, 2020, **152**, 47.
13. J. VandeVondele and J. Hutter, *J. Chem. Phys.*, 2007, **127**, 9.
14. S. Goedecker, M. Teter and J. Hutter, *Phys. Rev. B*, 1996, **54**, 1703-1710.
15. C. Hartwigsen, S. Goedecker and J. Hutter, *Phys. Rev. B*, 1998, **58**, 3641-3662.
16. M. Krack, *Theor. Chem. Acc.*, 2005, **114**, 145-152.
17. C. Adamo and V. Barone, *J. Chem. Phys.*, 1999, **110**, 6158-6170.
18. S. Grimme, J. Antony, S. Ehrlich and H. Krieg, *J. Chem. Phys.*, 2010, **132**, 19.
19. S. Grimme, S. Ehrlich and L. Goerigk, *Journal of Computational Chemistry*, 2011, **32**, 1456-1465.

20. J. Heyd, G. E. Scuseria and M. Ernzerhof, *J. Chem. Phys.*, 2003, **118**, 8207-8215.
21. A. V. Krukau, O. A. Vydrov, A. F. Izmaylov and G. E. Scuseria, *J. Chem. Phys.*, 2006, **125**, 5.
22. M. Guidon, J. Hutter and J. VandeVondele, *J. Chem. Theory Comput.*, 2010, **6**, 2348-2364.
23. J. P. Perdew, K. Burke and M. Ernzerhof, *Phys. Rev. Lett.*, 1996, **77**, 3865-3868.
24. M. Y. Yang, U. Raucci and M. Parrinello, *Nat. Catal.*, 2023, **6**, 829-836.
25. Y. Z. Zhang, H. D. Wang, W. J. Chen, J. Z. Zeng, L. F. Zhang, H. Wang and E. Weinan, *Comput. Phys. Commun.*, 2020, **253**, 11.
26. M. Y. Yang, L. Bonati, D. Polino and M. Parrinello, *Catal. Today*, 2022, **387**, 143-149.
27. S. Wille, H. Y. Jiang, O. Bünermann, A. M. Wodtke, J. Behler and A. Kandratsenka, *Phys. Chem. Chem. Phys.*, 2020, **22**, 26113-26120.
28. M. Kulichenko, B. Nebgen, N. Lubbers, J. S. Smith, K. Barros, A. E. A. Allen, A. Habib, E. Shinkle, N. Fedik, Y. W. Li, R. A. Messerly and S. Tretiak, *Chem. Rev.*, 2024, **124**, 13681-13714.